Structures quasi-accord de phase 3D : étude théorique, élaboration de matériaux non-linéaires, et réalisation des structures en matériau polymère

Tamara Pogosian

Thèse de doctorat

NNT : 2020UPASN007

3D nonlinear quasi-phase matching structures: theoretical analysis, material synthesis and study of polymer-based fabrication technique

Thèse de doctorat de l'université Paris-Saclay

École doctorale n°575 : electrical, optical, bio-physics and engineering (EOBE)
Spécialité de doctorat: physique
Unité de recherche : LPQM
Référent : ENS Paris-Saclay

Thèse présentée et soutenue à St. Petersburg, le 18/02/2020, par

Tamara POGOSIAN

Composition du Jury

Nikolay NIKONOROV Professeur, ITMO University	Président
Sébastien BIDAULT Chargé de Recherche, Institut Langevin	Rapporteur & Examinateur
Alexander SHKURINOV Professeur, Lomonosov Moscow State University	Rapporteur & Examinateur
Isabelle LEDOUX-RAK Professeur, ENS Paris-Saclay (UMR 8537)	Examinatrice
Ngoc Diep LAI Maître de Conférences, ENS Paris-Saclay (UMR 8537)	Directeur de thèse
Igor DENISYUK Professeur, ITMO University	Co-Directeur de thèse

Résumé

Dans ce travail, nous explorons théoriquement et expérimentalement des structures non-linéaires en trois dimensions (3D). Tout d'abord, nous avons étudié la théorie de quasi-accord de phase (QPM) des structures 3D pour une génération efficace de seconde-harmonique. L'efficacité de la conversion de fréquence est analysée en fonction de plusieurs paramètres, tels que le type de structures, le facteur de remplissage, le motif de maille, etc. Une structure QPM 3D optimale et très proche de la structure expérimentale a été démontrée. Ensuite, nous avons étudié plusieurs méthodes pour synthétiser des matériaux non-linéaires à base de cristaux de DAST. En particulier, la taille de ces cristaux a été optimisée en dessous de micromètre afin de les incorporer facilement dans des structures de polymère. Finalement, nous avons développé plusieurs méthodes pour créer des structures QPM 2D et 3D du type +/0 à la demande. La première méthode est basée sur la technique d'interférence de deux faisceaux laser, qui permet de pousser les cristaux DAST non-linéaires dans les zones sombres de la figure d'interférence. Cette technique rapide mais le contraste de

la propriété non-linéaire est faible. La deuxième méthode consiste à utiliser la technique dite écriture directe par laser. Cette méthode permet de blanchir la propriété des cristaux de DAST par l'effet photothermique local. En déplaçant le spot de focalisation du faisceau laser, n'importe quelle structure QPM 2D peut-être réalisée. Finalement, nous avons démontré une méthode rapide permettant d'obtenir des structures QPM 2D et 3D de grande contraste, en remplissant les trous de structures de SU-8, fabriquées initialement par la méthode d'interférence, par les cristaux DAST.

Abstract

In this study, we investigate theoretically and experimentally 3D quasi-phase matching (QPM) structures. The work focuses on i) mathematical analysis of second-harmonic generation efficiency in 3D QPM lattices, ii) synthesis and analysis of polymers materials with embedded nonlinear submicron particles for fabrication of nonlinear lattices, iii) development of methods for creation of nonlinear 2D and 3D QPM lattices. The purpose of the theoretical part is to define the influence of different parameters of 3D QPM structures on the efficiency of the frequency conversion. In order to conduct our experimental research, we then synthesis two composite materials which consist of polymer matrices with embedded nonlinear submicron DAST crystals. Using these materials, we are capable of creating novel methods of fabrication of 2D and 3D QPM structures. The first method consists of holographically writing a photopolymerizable composite, during which the nonlinear DAST crystals are transferred into the dark zones of the interference pattern. The second method employs the direct laser writing technique to patterning the submicron DAST crystals embedded in

polymer matrices, by the photothermal destruction effect. Finally, the third method allows creation of 2D nonlinear lattices by filling voids of SU-8 template with submicrometer DAST crystals.

Acknowledgements

First of all I would like to express my sincerest and deepest gratitude to my supervisors, Prof. Igor Denisyuk from ITMO University (Russia) and Prof. Ngoc Diep Lai from ENS Paris-Saclay (France). I am deeply grateful for their support of my PhD research, for their patience and knowledge.

Also I would like to express my sincere thanks and immense gratitude to professors, colleagues and labmates from both laboratories, Quantum and Molecular Photonics Laboratory (France) and Nonlinear optical molecular crystals and microlasers (Russia). I really appreciate all the advices and help with my research. It has been a true pleasure working with all of them.

More than that I am grateful for financial support provided by Embassy of France in Russia, ENS Paris-Saclay and ITMO University.

Finally, I must express my very profound gratitude to my family. This support can hardly be exaggerated.

Thank you.

List of publications (related to this work)

- **Pogosian T.N.**, Lai N.D. *"Theoretical investigation of three-dimensional quasi-phase-matching photonic structures"*, Physical Review A, Vol. 94 (6), pp. 063821 (2016)

- **Pogosian T.N.**, Mai T.N.A., Denisyuk I.Yu., Lai N.D. *"Synthesis and nonlinear optics characterization of DAST submicron crystals in polymerized thin films"*, Proceedings of SPIE, Vol. 10681, pp. 106811A (2018)

- **Pogosian T.N.**., Denisyuk I.Yu., Lai N.D. *"The influence of dimensional parameters of DAST nanocrystals on their linear and nonlinear optical parameters"*, Optics and spectroscopy, Vol. 126, No. 3, pp. 262-264 (2019)

- **Pogosian T.N.**, Denisyuk I.Yu., Lai N.D. *"Controllable synthesis of DAST submicron crystals and their microstructuration by direct laser writing"*, FIR-LAB 2019 Workshop & RJUSE Symposium proceedings, pp. 38-39 (2019)

Conference contributions

- **Pogosian T.N.**, Denisyuk I.Yu., Lai N.D. *"Controllable synthesis of DAST submicron crystals and their microstructuration by direct laser writing"*, 2nd Workshop of International Research Network FIR-LAB, Nizhny Novgorod (Russia), 2019. Oral.

- **Pogosian T.N.**, Mai T.N.A., Denisyuk I.Yu., Lai N.D. *"Synthesis and nonlinear optics characterization of DAST submicron crystals in polymerized thin films"*, SPIE Photonics Europe 2018, Strasbourg, 2018. Poster.

- **Погосян Т.Н.**, Денисюк И.Ю., Лай Н.Д.. *"Теоретическое и экспериментальное представление о трехмерных нелинейных структурах с фазовой квазисинхронизацией"*, X международная конференция молодых ученых и специалистов "Оптика 2017", Saint-Petersburg (Russia), 2017. Poster

- **Погосян Т.Н.**, Денисюк И.Ю. *"Теоретическое представление о трехмерных нелинейных структурах с фазовой квазисинхронизацией и способы их создания"*, КМУ ИТМО 2017, Saint-Petersburg, Russia, 2017. Oral.

Contents

Chapter 1

Introduction

1.1 Nonlinear optics: history, development and applications

The first experiment in nonlinear optics was demonstrated in 1961 [1] after the invention of the laser in 1960 [2]. It is connected with revealed potentials of lasers to achieve an electric field E of the light comparable to the intratomic electric field of the material [3].

Pioneers of this branch of science are Niclaas Bloembergen, who described theoretical basis of many nonlinear processes in the monograph "Nonlinear Optics"[4] and his doctoral student Yuen-Ron Shen, who wrote the book "The principles of nonlinear optics"[5].

Nowadays nonlinear optics have a huge amount of discovered effects such as collinear and noncollinear second harmonic generation

(SHG) [6], simultaneous wavelength interchange [7], third- and fourth-harmonic generations [8, 9], all-optical deflections and splitting [10], optical parameter oscillation [11], various beam shaping [12], laser wavelength extension [13], quantum light sources [14, 15] and terahertz technology [16, 17]. An essential condition in the most of these processes is the synchronization of the phases of the interacting waves, which is problematical due to the natural dispersion of materials.

There are two quite popular methods to overcome the phase mismatching, which induces the destructive interference of the new light generated in different regions of the nonlinear material. The first method uses the birefringence property of the nonlinear medium. Indeed, birefringent crystals have been used for minimizing the phase mismatching of frequency conversion since the early 1960s [18, 19]. These crystals provide equal refractive index for pair of wavelengths (fundamental and newly generated ones), thus resulting in a phase matching between these wavelengths. Unfortunately, this method has several insuperable drawbacks. First of all, not all phase-matching conditions can be satisfied due to the lack of proper crystal orientation. Second, birefringent crystals are very sensitive to temperature variations with a tolerance less than 0.1°C. Besides, most birefringent crystals have a limitation of efficient length due to the "walk-off" effect [20, 21, 22], thus it limits nonlinear conversion efficiency.

An alternative method involves a spatial modulation of the second-order nonlinear coefficient, $\chi^{(2)}$, in nonlinear material [23, 24]. It is

called quasi-phase matching (QPM) method and allows overcoming phase mismatching for any nonlinear process and for any nonlinear crystal (isotropic or anisotropic), by choosing an appropriate modulation periodicity. Despite popularity and advantages of this method, the fabrication of QPM structures remains as a big challenge. In particular, 3D QPM structures give the full potential of the QPM technique but until now, no way has been proposed to realize these structures on demand.

1.2 Quasi-phase matching structures

Figure 1.1 clearly shows difference between three cases for SHG: perfect phase matching, no phase matching and periodic 1D QPM. The condition for perfect phase matching is $k_{2\omega} - 2k_{\omega} = 0$, where k_{ω} and $k_{2\omega}$ are wave vectors for frequencies ω and ω respectively. The condition for phase mismatching is $k_{2\omega} - 2k_{\omega} \neq 0$. As it was mentioned, phase mismatching is a typical situation for nonlinear material due to the dispersion of materials. Phase mismatching wave vector is $\Delta k = k_{2\omega} - 2k_{\omega}$ and it can be compensated by a nonlinear grating, a QPM crystal. This QPM structure can be created by a spatial modulation of the material polarization. The period of the QPM structure depends on the coherence length between fundamental and generating wavelengths. Figure 1.1 shows how the nonlinear grating supports accumulation of new wave generation in k-vector scheme, evolution of the second harmonic

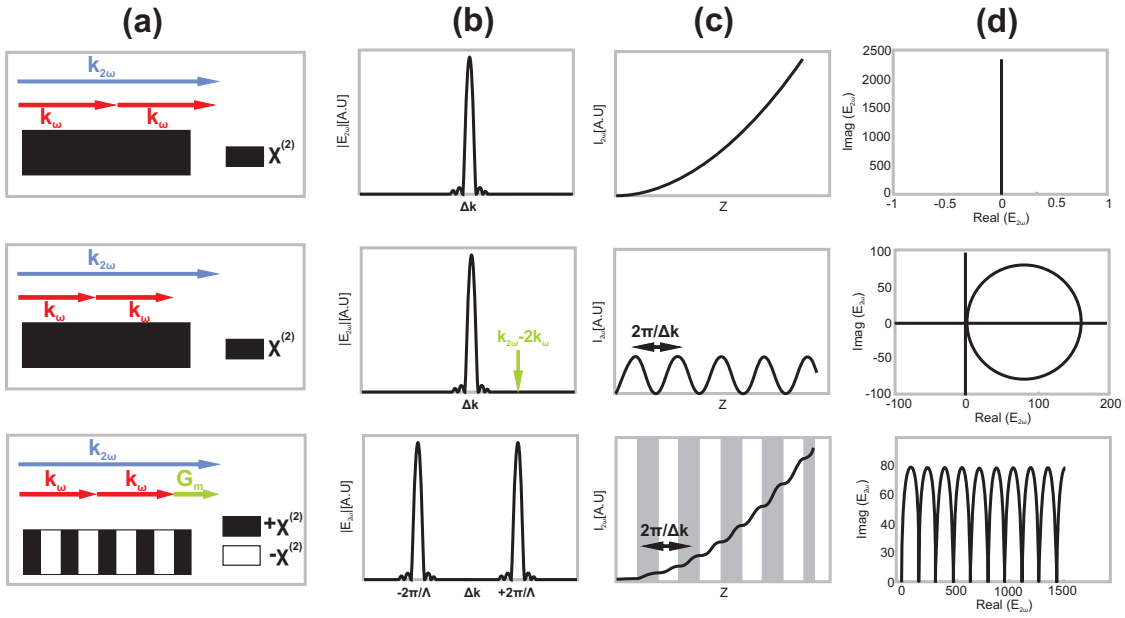

Figure 1.1: Phase matched, non-phase matched and (1D periodic) quasi-phase matched cases. From left to right: a) Nonlinearity along the crystal and k-vector scheme; b) Absolute value of the second-harmonic field vs. the spatial frequency; c) Evolution of the second-harmonic intensity along the crystal; d) Phasor diagram of the second-harmonic wave [26].

intensity and phasor diagram.

The QPM method has a lot of advantages. First of all, it can work with a wide range of nonlinear processes, at a convenient temperature and without spatial walk-off. Second, this method can utilize the largest nonlinear coefficient of the nonlinear material that is not possible with the birefringent method. Third, periodically poled crystals may have a reduced tendency for photorefractive damage [25].

Nowadays, a great number of 1D [24] and 2D [27] QPM structures are available. They differ by materials, fabrication techniques, types of light propagation and applications. The development of QPM tech-

nique provides a big amount of solutions to achieve higher nonlinear conversion efficiency. In order to increase the number of nonlinear processes in the same crystal, 1D and 2D QPM structures can be built using Fibonacci-based order [28], dual-grid method [26], blocks built in quasi-periodic order [29], super QPM [30], and randomized order for broadband generation [31].

Different kinds of nonlinear materials require different fabrication techniques for realization QPM structures. For example, an electric poling method has been used successfully to pole various ferroelectric crystals ($LiNbO_3$, $LiTaO_3$, $KTiOPO_4$, etc.) for 1D [32] and 2D [8] QPM structures. However, the idea to apply a high voltage via a patterned electrode to reverse the sign of nonlinear coefficient faces a problem of fabrication a 3D QPM structure. Another fabrication technique is based on selectively growing of nonlinear semiconductors such as GaAs [33], and provides large nonlinearity and extensive transparency. However, it is also not applicable in creating 3D QPM structures. Also very promising type of nonlinear materials are polymers. It proves a list of fabrication techniques, such as UV photo bleaching [34], photothermal poling [35], periodic poling [36], all-optical poling [37], photodepoling with photolithographic masks [38], two-beam interference [39], and direct laser writing [40, 41].

It is worth mentioning that QPM can be achieved by reversing the sign of domains with a periodicity determined by the coherence length of the nonlinear crystal or by modulation of the nonlinear material

with a linear material, which possesses a $\chi^{(2)}$ null. The first method is more efficient, because it uses full length of crystal to accumulate generation while the second method aborts generation in the areas with nullified $\chi^{(2)}$. We can call these two types of QPM as "+/- "QPM and "+/0 "QPM respectively. For 1D and 2D cases "+/- "QPM is more preferable because of its efficiency. However we suppose that in 3D case "+/0 "QPM is the best choice. Our opinion is motivated by the fact that if an electric field of the fundamental light beam stands perpendicular to polarization of dipoles and hence polarization of material, it results in an absence of nonlinear effect. It means that one direction of material is totally no use, and that is prohibitive for 3D QPM. Therefore the best option is randomly oriented domains with strong nonlinear coefficient which are spatially distributed in linear material.

1.3 Theoretical approach for QPM structures

Investigation of 1D and 2D QPM structures allows to conclude that there is a clear advantage to increase the number of reciprocal vectors. Extension in the third dimension will give exclusive access for phase matching of nonlinear processes along an arbitrary direction. At the presence, it is hard to predict which additional effects can provide 3D

QPM and it is underexplored branch of nonlinear optics because of fabrication difficulties. Hence it is worth investigating.

The aim of this research work is theoretical investigation of 3D QPM structures and its practical realization using polymer-based materials. Concerning publications devoted to theoretical part there are few researches [42, 43, 26] which show general approach to QPM structures and one is presented by our group [44]. This research work uses Fourier transform approach, which was well described for 1D QPM structures in Reference [24] and then for 2D QPM structures in Reference [45]. Our aim is to extend this approach to 3D QPM structures and use it for analytical analysis of the nonlinear conversion efficiency of such structures.

This approach analyzes SHG as the prototypical second-order interaction and studies efficiency of this process as a function of different parameters of the structure. It uses typical assumptions to simplify calculations of SH amplitude, such as no losses for fundamental or second SH waves and slowly varying amplitude approximation.

Theoretical model of 3D QPM structure should represent spatial modulation of nonlinear coefficient function. Periodical function can be described as domains, which has $\chi^{(2)}$ with a negative sign and are located in points of Bravais lattice. The surrounding material possesses a $\chi^{(2)}$ with a negative sign. Thus 3D QPM is presented as convolution product of lattice and motif. That is convenient model for Fourier transform approach.

1.4 Fabrication of 3D QPM

Fabrication of 3D QPM structures is a difficult technological task. There were few attempts to do that using formation of 3D nonlinear photonic lattices in cerium doped strontium barium niobate (SBN:Ce) photorefractive material by a spatial light modulator (SLM)-assisted versatile single step optical induction approach [46], direct laser writing method with Disperse Red 1 (DR1) sol-gel polymer [47] and DR1-Poly-methyl-methacrylate copolymer [48]. It is worth mentioning a recent success with $Ba_{0.77}Ca_{0.23}TiO_3$ (BCT) crystal, which firstly was found naturally grown [49] and used for broadband 3D QPM and then was used to fabricate a 3D nonlinear photonic crystal by applying an ultrafast light domain inversion approach [50]. Very recently, 3D QPM structure has been fabricated by using a femtosecond laser to selectively erase the nonlinear coefficients in a $LiNbO_3$ crystal [51].

Closer look to these attempts indicates that earlier researches showed time-consuming fabrication techniques. For example the authors of Reference [48] used layer-by-layer direct laser writing technique, which requires spincoating of different materials layer by layer (Figure 1.2). Ultrafast light domain inversion approach [50], where the nonlinear absorption of light results in a high temperature of the material in the laser focus and leads to induced bipolar thermoelectric field which reorient random domains into two large antiparallel domains (Figure 1.4), is also time consuming and requires a femto-second laser and

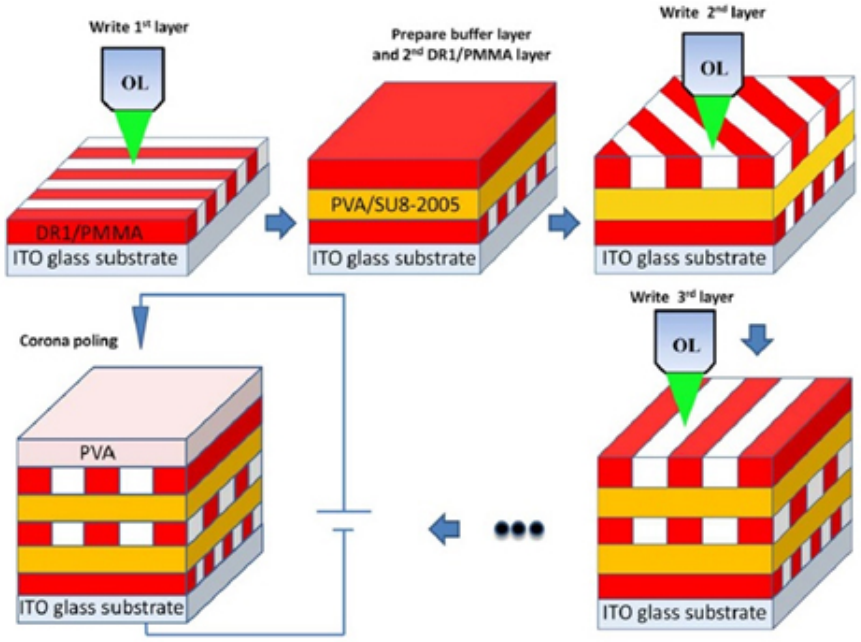

Figure 1.2: Fabrication process of 3D polymer quadratic nonlinear grating by layer-by-layer direct laser writing technique [48].

complicated optical system.

The aim of this research is to find alternative ways of fabrication connected with interference techniques to rapidly obtain uniform structures over large area. This work is therefore focused on investigating polymers as a promising material for fabrication of 3D QPM structures, because this material is well adapted to holographic techniques. The aim is to fabricate QPM structure with "+/0 "modulation of $\chi^{(2)}$ using a spatial distribution of embedded submicron nonlinear crystals in polymer matrix. For this purpose a well-known highly nonlinear 4-[4-(Dimethylamino)styryl]-1-methylpyridinium p-toluenesulfonate (DAST) crystals were chosen.

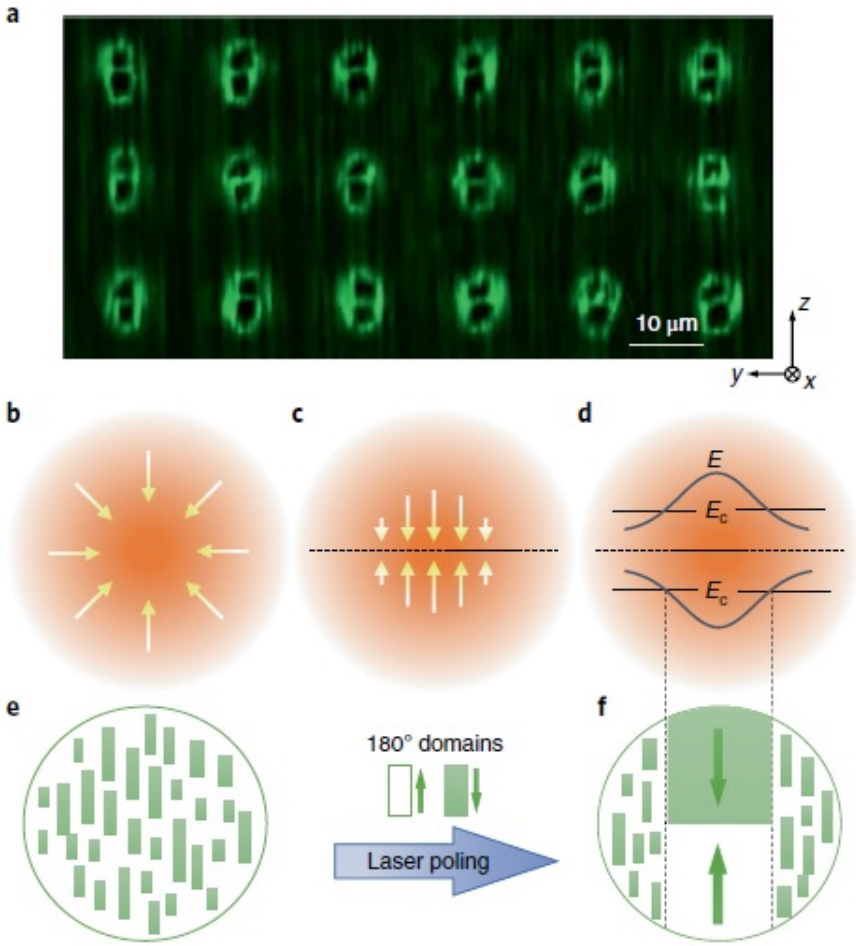

Figure 1.3: Fabrication process of 3D QPM structure by ultrafast light domain inversion approach [50].

1.5 DAST crystals: properties and submicron fabrication

DAST is a salt composed by a stilbazolium cation, one of the most efficient NLO active chromophores and the tosylate (anion), which induces the noncentrosymmetric macroscopic crystal packing. In Fig-

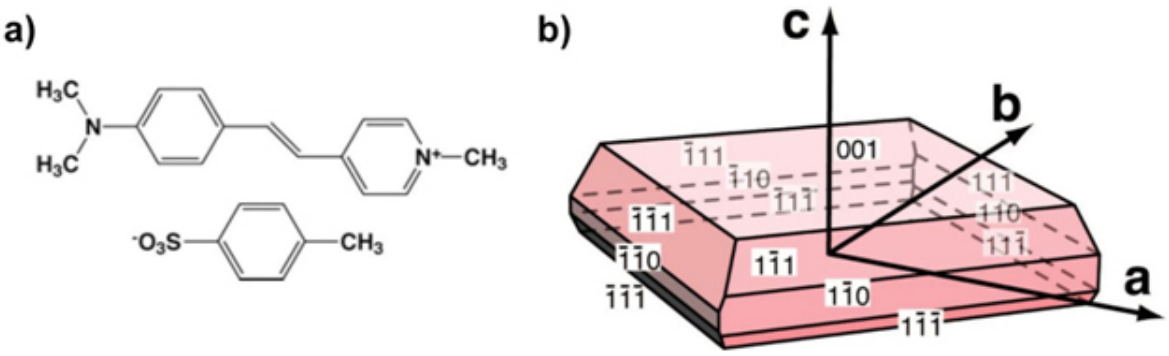

Figure 1.4: a) Molecular diagram of DAST and b) growth habit of DAST crystals grown from methanol. The fastest growth direction is along the crystallographic a or [100] direction [52].

ure 1.4 you can see molecular diagram of DAST and growth habit of DAST crystals grown from methanol, taken from the Reference [52].

According to the Reference [53], DAST can have several crystalline forms depending on packing of molecules and on environment influence. We can mention three of them, even there exists other less-known forms. One of the forms is an orange color needle-like single crystal. This crystal is centrosymmetric and do not have $\chi^{(2)}$ nonlinear properties. Green–red color rough surface polycrystal and green–red color ordered surface single crystal are non-centrosymmetric types of packing and hence show $\chi^{(2)}$ nonlinear properties. For example green–red color ordered surface single crystal exhibits a very large second-order NLO susceptibility, $\chi^2 = 2020 \pm 220$ pm/V at $\lambda = 1318$ nm and electro-optical figure of merit $n_1^3 r_{11} = 530 \pm 60$ pm/V at $\lambda = 1318$ nm [52]. Hence DAST crystals are known as highly nonlinear material.

In case of organic nonlinear crystals it should be taken into consid-

eration a well-known fact that the presence of water molecules within the crystal structure leads to a network of hydrogen bonds [54]. Hence the water molecules and tosylate anions form centrosymmetric O–H. . . O hydrogen-bonded rings. That leads to a centrosymmetry of crystals and to loss the nonlinear properties. Water is also a strong solvent for DAST crystals. It means that insertion of water into solutions should be avoided for correct growth of DAST nonlinear crystals.

As it was mentioned before, submicron DAST crystals are required for realization of 2D and 3D QPM structures. Concerning this demand, a few publications are devoted to synthesis of DAST nanocrystals. The first strategy for adjusting the kinetic growth process of organic nanocrystals is to use the size-isolation effect of dendrimers [55, 56]. Depending on synthesis conditions the size of DAST crystals varies from 50 nm to 200 nm. The second method of growing DAST nanocrystals allows obtaining liquid dispersions of organic nanocrystals with size and shape controlled by experimental conditions [57, 58]. DAST-ethanol solution is injected into vigorously stirred decalin at room temperature. The surfactant of n-dodecyltrimethylammonium chloride is added to avoid aggregation between DAST nanocrystals.

This work follows the third method, described in articles devoted to synthesis of DAST crystals in PMMA matrix [59, 60]. This method consists of several steps, which are preparation of DAST/polymer (or monomer) solution, spincoating of solution on the substrate and thermal annealing of a sample. This process is easy for realization and

time-saving.

1.6 Conclusion

This research work consists of two big parts: theoretical and experimental. Chapter 2 is totally devoted to theoretical calculations. A theoretical model of 3D QPM structure is chosen and the nonlinear properties are calculated by the Fourier transform approach. This approach presented in Reference [24] for 1D QPM structure and in Reference [45] for 2D QPM structure. It allows analyzing the phase-matching characteristics of QPM structures by taking a Fourier transform of the nonlinear coefficient function traced out by the grating pattern. The Fourier transform can generate a map of available grating vectors in (wave vector mismatch) space or can present efficiency of particular structure depending on its parameters. Even this method has several limitations, mentioned in Chapter 2, it is very useful especially for analytical examination of simple periodical structures. Chapter 2 mainly deals with the analysis of SHG efficiency in 3D QPM structures, which differs by parameters of lattice and motifs.

Chapter 3 is devoted to experimental investigation of 2D and 3D QPM structures realization by using polymers materials. The main role is assigned to highly nonlinear DAST crystals. One of the chapter subsections investigates a possibility to synthesis submicron crystals of DAST and factors which influence on their form and properties.

Chapter 3 described three methods to dispose spatially and fix DAST crystals in polymer matrices or epoxy-based negative photoresist SU-8. As results, all methods were approved by 1D and 2D nonlinear structures and showed prospective possibilities to create 3D “+/0 ”QPM structures.

Chapter 2

Theoretical model of 3D QPM structures

2.1 Wave equations and model approximation of 3D QPM structures

This chapter is focused on theoretical calculation of collinear SHG. It can be used for other nonlinear wave mixing processes. The general theory was adapted from the Reference [26] and extended from 2D theoretical model of QPM structure to 3D QPM. Hence the electric fields in the QPM structure for fundamental harmonic with frequency ω and second-harmonic (SH) with frequency 2ω can be written as

$$\widetilde{E}_{\omega}(\mathbf{r},t)=\frac{1}{2}E_{\omega}(\mathbf{r})\exp\left[i\left(\omega t-\mathbf{k}_{\omega}\cdot\mathbf{r}\right)\right]+c.c., \tag{2.1}$$

$$\widetilde{E}_{2\omega}(\mathbf{r},t)=\frac{1}{2}E_{2\omega}(\mathbf{r})\exp\left[i\left(2\omega t-\mathbf{k}_{2\omega}\cdot\mathbf{r}\right)\right]+c.c., \tag{2.2}$$

where $\mathbf{r}\equiv(x,y,z)$ is the 3D spatial coordinates, $\mathbf{k}_{\omega}$ and $\mathbf{k}_{2\omega}$ are corresponding wave vectors of fundamental and SH frequencies, respectively.

Slowly varying amplitude approximation assumes that the relative change of the field envelopes $E_{\omega}(\mathbf{r})$ and $E_{2\omega}(\mathbf{r})$ over a propagation distance of a wavelength is small, hence $\nabla^2 E_{2\omega}(\mathbf{r}) << \mathbf{k}_{2\omega}\nabla E_{2\omega}(\mathbf{r})$. Besides, the fundamental amplitude is assumed constant throughout entire interaction length. Using these assumptions, the evolution of the fundamental and the SH field amplitudes can be written as:

$$\mathbf{k}_{\omega}\nabla E_{\omega}(\mathbf{r})=-2i\frac{\omega^2}{c^2}E_{2\omega}E_{\omega}^{*}d(\mathbf{r})\exp\left[-i\left(\mathbf{k}_{2\omega}-2\mathbf{k}_{\omega}\right)\mathbf{r}\right], \tag{2.3}$$

$$\mathbf{k}_{2\omega}\nabla E_{2\omega}(\mathbf{r})=-2i\frac{\omega^2}{c^2}E_{\omega}^{2}d(\mathbf{r})\exp\left[i\left(\mathbf{k}_{2\omega}-2\mathbf{k}_{\omega}\right)\mathbf{r}\right], \tag{2.4}$$

where E_{ω}^{*} is the complex conjugate of E_{ω}. $\mathbf{k}_{2\omega}-2\mathbf{k}_{\omega}=\triangle\mathbf{k}$ is a mismatching vector between wave vectors of SH and fundamental waves. $d(\mathbf{r})=\chi_{ijk}^{(2)}\cdot g(\mathbf{r})/2$ is a nonlinearity function and $g(\mathbf{r})$ is a normalized

and unitless function, representing space dependence of the nonlinear coefficient function. To find out the electric field, and hence the intensity of SH, the Eq. 2.4 can be directly integrated using numerical methods. This method can be applied for any periodic or aperiodic structure. However, the aim is to analyze efficiency of basic periodic QPM structures and to compare results of calculations with other works. Hence, it is convenient to use Fourier transform approach [24, 45].

Theoretically, 3D QPM structures can be modeled as a convolution between a periodic lattice and a nonlinear motif with a function $s(\mathbf{r})$ (Figure 3.19). Let's consider that a motif presents $\chi^{(2)}$ with a positive sign, "+1", while surrounding materials possess a $\chi^{(2)}$ with a negative sign "−1"or a null value ("0"). In this case, the nonlinear coefficient is presented as a Fourier series and the sum is extended over the whole 3D reciprocal lattice (RL):

$$g(\mathbf{r}) = \sum \mathbf{G}_{mnq} \cdot \exp\left(i\mathbf{K}_{mnq} \cdot \mathbf{r}\right). \tag{2.5}$$

Here $\mathbf{G}_{mnq}$ are Fourier coefficients and $\mathbf{K}_{mnq}$ are RL vectors (RLVs) which depend on orders m, n and q. Mismatching vector $\Delta\mathbf{k}$ can be compensated by one of RLVs, which will lead to a significant build-up of the SH power. Assuming that (m, n, q) order satisfies the condition of phase matching $\Delta\mathbf{k} - \mathbf{K}_{mnq} = 0$, all other orders contribute negligible oscillating terms. After an interaction length L the SH intensity can

be calculated as:

$$I_{2\omega} \approx \frac{2\omega^2 \chi^{(2)}_{ijk} \left|\mathbf{G}_{mnq}\right|^2}{n_{2\omega} n_\omega^2 c^3 \varepsilon_0} I_\omega^2 L^2, \tag{2.6}$$

with

$$\mathbf{G}_{mnq} = \frac{1}{V} \int s\left(\mathbf{r}\right) \exp\left(i\mathbf{K}_{mnq} \cdot \mathbf{r}\right) d^3\mathbf{r} = \frac{1}{V} S\left(\mathbf{K}_{mnq}/2\pi\right). \tag{2.7}$$

The Eq. 2.7 can be achieved by multiplication of both sides in Eq. 2.5 by $\exp\left(-i\mathbf{K}_{mnq} \cdot \mathbf{r}\right)$ and integration over an unit cell V. $S\left(\mathbf{f}\right)$ is Fourier transform of the motif. It is well seen that the Fourier coefficient depends on the type of lattice $\mathbf{K}_{mnq}$ and type of motif, $s\left(\mathbf{r}\right)$.

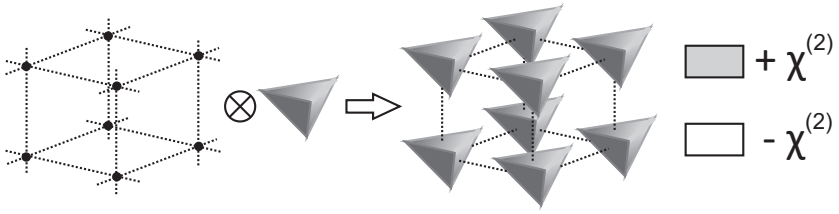

Figure 2.1: Convolution of a simple cubic lattice with a triangular motif to model 3D periodic QPM structures.

2.2 Influence of lattice. Real and reciprocal vectors

Mathematically, periodical QPM structure can be treated as regular periodical crystal. The 3D periodic crystals are classified by 14 types

of Bravais lattice grouped into 7 lattice systems: triclinic, monoclinic, orthorhombic, tetragonal, cubic, trigonal, and hexagonal [61]. An important point is that there are a lot of complicated structures appeared as combinations of simple structures, for example body-centered cubic (BBC), face-centered cubic (FCC) or diamond cubic (DC).

Three fundamental translation vectors, $\mathbf{a}_1$, $\mathbf{a}_2$ and $\mathbf{a}_3$, determine any 3D lattice. Hence all real lattice points $\mathbf{r}$ are defined by a set of arbitrary integers u_1, u_2 and u_3:

$$\mathbf{r} = u_1\mathbf{a}_1 + u_2\mathbf{a}_2 + u_3\mathbf{a}_3. \tag{2.8}$$

According to Figure 2.2, primitive vectors$\mathbf{a}_1$, $\mathbf{a}_2$ and $\mathbf{a}_3$ can be described by lengths a, b and c and by three angles α, β and γ. Let assume that $\mathbf{a}_1$ belongs to an x-axis, $\mathbf{a}_2$ lies in xy-plane and $\mathbf{a}_3$ is determined by all three axes, hence primitive vectors of a triclinic lattice can be represented as:

$$\mathbf{a}_1 = a\,(1, 0, 0)\,, \tag{2.9a}$$

$$\mathbf{a}_2 = b\,(\cos\gamma, \sin\gamma, 0)\,, \tag{2.9b}$$

$$\mathbf{a}_3 = c\,(\cos\beta, \cos\alpha\sin\gamma, \sin\alpha\sin\beta)\,. \tag{2.9c}$$

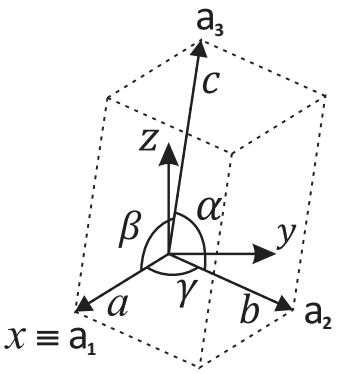

Figure 2.2: Triclinic unit cell with parameters defined in the text.

The volume of the unit cell can be calculated as $V = abc \sin\alpha \sin\beta \sin\gamma$. RLVs can be determined by using the relation $\mathbf{a}_i \cdot \mathbf{b}_j = 2\pi\delta_{ij}$, where δ_{ij} is Kronecker delta. Hence for general case in triclinic lattice, RLVs are:

$$\mathbf{b}_1 = \frac{2\pi}{a}\left(1, \frac{-1}{\tan\gamma}, \left(\frac{\cos\gamma}{\tan\alpha\sin\beta} - \frac{1}{\tan\beta\sin\alpha}\right)\right), \tag{2.10a}$$

$$\mathbf{b}_2 = \frac{2\pi}{b}\left(0, \frac{1}{\sin\gamma}, \frac{-1}{\tan\alpha\sin\beta}\right), \tag{2.10b}$$

$$\mathbf{b}_3 = \frac{2\pi}{c}\left(0, 0, \frac{1}{\sin\alpha\sin\beta}\right). \tag{2.10c}$$

While real lattice points $\mathbf{r}$ are presented by Eq. 2.8, the 3D reciprocal lattice points are given by:

$$\mathbf{K}_{mnq} = m \cdot \mathbf{b}_1 + n \cdot \mathbf{b}_2 + q \cdot \mathbf{b}_3. \tag{2.11}$$

Table 2.1 presents summarized parameters, primitive vectors, unit cell volume and RLVs for four 3D lattices: triclinic, orthorhombic, cubic and hexagonal.

2.3 Influence of motif. Orthorhombic spherical and cylindrical motifs

This section describes and analyzes the simplest motifs. However, any motif function $s(\mathbf{r})$ can be used in Eq. 2.7. Varying parameters of the motif allows one to investigate the conversion efficiency for a chosen QPM order. The conversion efficiency can achieve the highest value or null value, which is useful for nullifying unwanted processes. It should be pointed out that Fourier transform approach does not provide the correct result if nearby motifs overlap with each other.

Mathematically, the orthorhombic motif is defined by:

$$s(\mathbf{r}) = \mathrm{rect}\left(\frac{x}{X}\right)\mathrm{rect}\left(\frac{y}{Y}\right)\mathrm{rect}\left(\frac{z}{Z}\right), \tag{2.12a}$$

where

$$\mathrm{rect}(u) = \begin{cases} +1 & |u| \leq \frac{1}{2} \\ p & \text{elsewhere} \end{cases} \tag{2.12b}$$

Here value of p depends on the type of structure. For "+/-"QPM

structures, p is equal -1, and for "+/0"QPM structures, p is equal 0. We can calculate the corresponding Fourier transform as:

$$S(\mathbf{f}) = P \cdot (XYZ)[\mathrm{sinc}(f_x X)\,\mathrm{sinc}(f_y Y)\,\mathrm{sinc}(f_z Z)] \tag{2.13}$$

where the sinc-function is defined as $\mathrm{sinc}(x) = \sin(x)/x$; X, Y and Z are a size of three sides of the orthorhombic motif. P=2 for "+/–"QPM structures; and P=1 for "+/0"QPM structures. It should be noted that coefficients which are calculated for "+/-"structures are twice larger than coefficients for "+/0"structures. Table 2.2(a) displays the Fourier coefficients of the orthorhombic motif for four types of lattice calculated for "+/-"QPM structures.

Concerning the equations in Table 2.2(a), there are some limitations connected with overlapping of motifs in Fourier transform approach. Thus, in case of orthorhombic and square lattices, the side of the motif should not exceed the side of the unit cell, i.e$X/a \leq 1$. Obviously, there is no need to present all possible coefficients for each QPM-order due to the knowledge of the sinc-function, which can allow distinguishing the highest values analytically.

In the orthorhombic lattice, the highest coefficient is $|\mathbf{G}_{100}|^2 = 0.405$. This coefficient is achieved for the first order $(m, n, q) = (1, 0, 0)$ with following parameters: $X/a = 0.5$, $Y/b = 1$ and $Z/c = 1$. Indeed, it is a 1D-like structure (Figure 2.3a) and the result is very consistent with the results published in Reference [26]. Similarly, the second

Table 2.1: Parameters, primitive vectors, unit cell volume and RLVs for four particular 3D lattices

	Triclinic	Orthorhombic	Cubic	Hexagonal
Parameters	$a \neq b \neq c$	$a \neq b \neq c$	$a = b = c$	$a = b \neq c$
	$\alpha \neq \beta \neq \gamma$	$\alpha = \beta = \gamma = 90°$	$\alpha = \beta = \gamma = 90°$	$\alpha = \beta = 90°, \gamma = 120°$
Primitive	$\mathbf{a}_1 = a\,(1, 0, 0)$	$\mathbf{a}_1 = a\,(1, 0, 0)$	$\mathbf{a}_1 = a\,(1, 0, 0)$	$\mathbf{a}_1 = a\,(1, 0, 0)$
vectors	$\mathbf{a}_2 = b\,(\cos\gamma, \sin\gamma, 0)$	$\mathbf{a}_2 = b\,(0, 1, 0)$	$\mathbf{a}_2 = a\,(0, 1, 0)$	$\mathbf{a}_2 = a\left(-\frac{1}{2}, \frac{\sqrt{3}}{2}, 0\right)$
	$\mathbf{a}_3 = c\,(\cos\beta, \cos\alpha\sin\gamma, \sin\alpha\sin\beta)$	$\mathbf{a}_3 = c\,(0, 0, 1)$	$\mathbf{a}_3 = a\,(0, 0, 1)$	$\mathbf{a}_3 = c\,(0, 0, 1)$
Unit cell volume	$V = abc\sin\alpha\sin\beta\sin\gamma$	$V = abc$	$V = a^3$	$V = a^2 c\frac{\sqrt{3}}{2}$
RLVs	$\mathbf{b}_1 = \frac{2\pi}{a}\left(1, \frac{-1}{\tan\gamma}, \left(\frac{\cos\gamma}{\tan\alpha\sin\beta} - \frac{1}{\tan\beta\sin\alpha}\right)\right)$	$\mathbf{b}_1 = \frac{2\pi}{a}\,(1, 0, 0)$	$\mathbf{b}_1 = \frac{2\pi}{a}\,(1, 0, 0)$	$\mathbf{b}_1 = \frac{2\pi}{a}\left(1, \frac{1}{\sqrt{3}}, 0\right)$
	$\mathbf{b}_2 = \frac{2\pi}{b}\left(0, \frac{1}{\sin\gamma}, \frac{-1}{\tan\alpha\sin\beta}\right)$	$\mathbf{b}_2 = \frac{2\pi}{b}\,(0, 1, 0)$	$\mathbf{b}_2 = \frac{2\pi}{a}\,(0, 1, 0)$	$\mathbf{b}_2 = \frac{2\pi}{a}\left(0, \frac{2}{\sqrt{3}}, 0\right)$
	$\mathbf{b}_3 = \frac{2\pi}{c}\left(0, 0, \frac{1}{\sin\alpha\sin\beta}\right)$	$\mathbf{b}_3 = \frac{2\pi}{c}\,(0, 0, 1)$	$\mathbf{b}_3 = \frac{2\pi}{a}\,(0, 0, 1)$	$\mathbf{b}_3 = \frac{2\pi}{c}\,(0, 0, 1)$

Table 2.2: Fourier coefficient of (a) an orthorhombic motif and (b) a spherical motif for "+/-"structures

Lattice type	Fourier coefficients
(a) Fourier coefficient of an orthorhombic motif	
Triclinic	$\mathbf{G}_{mnq} = \frac{2XYZ\mathrm{sinc}\left(m\frac{X}{a}\right)\mathrm{sinc}\left(Y\frac{an-bm\cos\gamma}{ab\sin\gamma}\right)\mathrm{sinc}\left(Z\frac{abq-acn\cos\alpha+cbm(\cos\alpha\cos\gamma-\cos\beta)}{abc\sin\alpha\sin\beta}\right)}{abc\sin\alpha\sin\beta\sin\gamma}$
Orthorhombic	$\mathbf{G}_{mnq} = 2\frac{XYZ}{abc}\mathrm{sinc}\left(m\frac{X}{a}\right)\mathrm{sinc}\left(n\frac{Y}{b}\right)\mathrm{sinc}\left(q\frac{Z}{c}\right)$
Square	$\mathbf{G}_{mnq} = 2\frac{XYZ}{a^3}\mathrm{sinc}\left(m\frac{X}{a}\right)\mathrm{sinc}\left(n\frac{Y}{a}\right)\mathrm{sinc}\left(q\frac{Z}{a}\right)$
Hexagonal	$\mathbf{G}_{mnq} = 2\frac{XYZ}{a^2c\sqrt{3}}\mathrm{sinc}\left(m\frac{X}{a}\right)\mathrm{sinc}\left((m+2n)\frac{Y}{a\sqrt{3}}\right)\mathrm{sinc}\left(q\frac{Z}{c}\right)$
(b) Fourier coefficient of a spherical motif	
	$\mathbf{G}_{mnq} = \frac{8\pi}{\lvert\mathbf{K}\rvert^3V}\left(\sin\left(\lvert\mathbf{K}\rvert R\right) - \lvert\mathbf{K}\rvert R\cos\left(\lvert\mathbf{K}\rvert R\right)\right)$
Triclinic	$\lvert\mathbf{K}\rvert = 2\pi\sqrt{\frac{m^2}{a^2} + \frac{(an-bm\cos\alpha)^2}{a^2b^2(\sin\gamma)^2} + \frac{(abq-acn\cos\alpha+cbm(\cos\alpha\cos\gamma-\cos\beta))^2}{a^2b^2c^2(\sin\alpha\sin\beta)^2}}$
Orthorhombic	$\lvert\mathbf{K}\rvert = 2\pi\sqrt{\frac{m^2}{a^2} + \frac{n^2}{b^2} + \frac{q^2}{c^2}}$
Square	$\lvert\mathbf{K}\rvert = \frac{2\pi}{a}\sqrt{m^2+n^2+q^2}$
Hexagonal	$\lvert\mathbf{K}\rvert = 2\pi\sqrt{\frac{4(m^2+mn+n^2)}{3a^2} + \frac{q^2}{c^2}}$

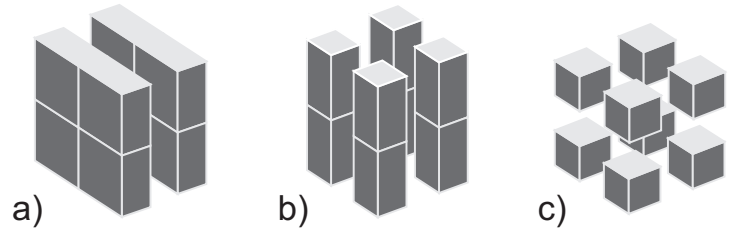

Figure 2.3: (a) 1D-like structure with parameters $X/a = 0.5$, $Y/b = 1$ and $Z/c = 1$; (b) 2D-like structure with parameters $X/a = 0.5$, $Y/b = 0.5$ and $Z/c = 1$; (c) 3D structure with parameters $X/a = 0.5$, $Y/b = 0.5$ and $Z/c = 0.5$.

QPM order $(1, 1, 0)$ relies on two primitive vectors and has the most efficient coefficient $|\mathbf{G}_{110}|^2 = 0.041$. Here, a 2D QPM structure was obtained (Figure 2.3b). A new QPM order $(1, 1, 1)$ which appears in 3D structures (Figure 2.3c) relies on all three primitive vectors. It has the highest value $|\mathbf{G}_{111}|^2 = 0.004$ with parameters $X/a = 0.5$, $Y/b = 0.5$ and $Z/c = 0.5$.

Note that in 3D QPM structures, the propagation direction of the fundamental light beam through the nonlinear crystal plays a big role. The SHG direction is determined by the QPM order. Let fix the structure as it is shown in Figure 2.3c and analyze difference of efficiency for different QPM orders. First order $(1, 0, 0)$ has a coefficient $|\mathbf{G}_{100}|^2 = 0.025$ which is 16 times smaller than coefficient for 1D-like structure in Figure 2.3a. This is the result of the 4 times less working material comparing with 1D-like structure, leading to a 4×4 times weaker nonlinear coefficient. Similar thing occurs with order $(1, 1, 0)$. $|\mathbf{G}_{110}|^2 = 0.010$ corresponds to 3D QPM structure and it is 4 times smaller than the coefficient for 2D-like structure due to 2 times less

working material.

Now, let's consider a spherical motif, which can be determined as:

$$s(\mathbf{r}) \equiv \begin{cases} +1 & |\mathbf{r}| \leq R \\ p & \text{elsewhere} . \end{cases} \tag{2.14}$$

Here the spherical motif has a radius R and $\chi^{(2)} = 1$ immersed in a background with $\chi^{(2)} = p$, where p is equal -1 in case of "+/- "QPM structures and p is equal 0 in case of "+/0"QPM structures. The corresponding Fourier transform can be obtained as:

$$S(\mathbf{f}) = \frac{4\pi P}{|\mathbf{f}^3|} \left(\sin(|\mathbf{f}| R) - |\mathbf{f}| R \cos(|\mathbf{f}| R)\right) \tag{2.15}$$

where, similar to orthorhombic motif, $P = 2$ for "+/-"QPM structures and $P = 1$ for "+/0"QPM structures.

Table 2.2(b) reports Fourier coefficients of the sphere motif for four types of lattice. Note that in case of the cubic lattice the value of Fourier coefficients can be analyzed as a function of the ratio between spherical radius and length of primitive vector $\mathbf{G}_{mnq}(R/a)$, where ratio R/a should not exceed 0.5. In case of the orthorhombic lattice, the dependence is more complicated. Here, the Fourier coefficient can be analyzed as a function $\mathbf{G}_{mnq}(R/a; a/b; a/c)$, where a corresponds to the length of the shortest primitive vector. For correct results, the Fourier transform approach requires conditions: $R/a \leq 0.5$, $a/b \leq 1$

and $a/c \leq 1$.

The analysis of the orthorhombic lattice with spherical motifs showed that the highest coefficients for the first QPM orders are not equal. If fundamental light propagates along the shortest primitive vector (Figure 2.3a), a maximum nonlinear coefficient of the first order, which can be achieved, is $|\mathbf{G}_{100}|^2 = 0.159$ with parameters $R/a = 0.5$, $a/b = 1$ and $a/c = 1$. Formally, this is a particular case of a cubic lattice where all first orders are equal, $|\mathbf{G}_{100}|^2 = |\mathbf{G}_{010}|^2 = |\mathbf{G}_{001}|^2 = 0.159$. That means that the conversion efficiency is equal in all three directions.

However, in orthorhombic lattice, first orders $(0, 1, 0)$ (Figure 2.3b) or $(0, 0, 1)$ (Figure 2.3c) provide significantly higher efficiency $|\mathbf{G}_{010}|^2 = |\mathbf{G}_{001}|^2 = 0.190$ with parameters $R/a = 0.5$, $a/b = 0.65$ and $a/c = 1$. These results have a good agreement with analysis of a rectangular lattice and circular motifs reported in Reference [62]. On closer examination, it is obvious that rows of circular motifs aim to shape and period of the most efficient 1D structure (Figure 2.5a) as well as rows of spheres aim the same structure (Figure 2.5b). Although they are not similar, we can compare their efficiency. We have already shown that the highest nonlinear coefficient for the rectangular motif in a rectangular lattice (2D) and the orthorhombic motif in an orthorhombic lattice (3D) is $|\mathbf{G}_{10}|^2 = |\mathbf{G}_{100}|^2 = 0.405$ and it is the same as that of a 1D structure. The highest normalized efficiency for a rectangular lattice with a circular motif is $|\mathbf{G}_{10}|^2 = 0.338$ with parameters $R/a_2 = 0.5$ and $R/a_1 = 0.29$ [62] and it is very close to the value 0.405. As it is

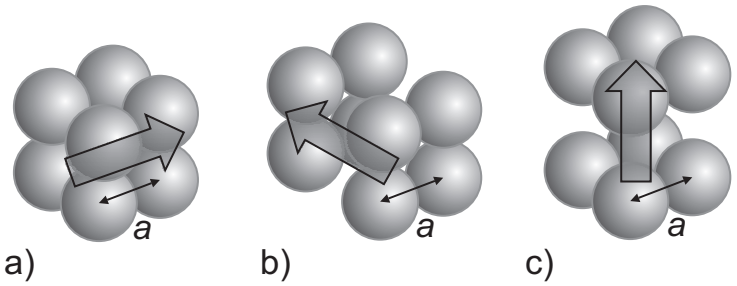

Figure 2.4: Optimum configurations of a 3D QPM structure with orthorhombic lattice, spherical motif, and the shortest side a depending on QPM order: a) $(1, 0, 0)$ order for collinear QPM means that the fundamental light propagates along the shortest side of the lattice, b) $(0, 1, 0)$ and c) $(0, 0, 1)$ orders both have propagation of the fundamental light in perpendicular direction to the shortest side.

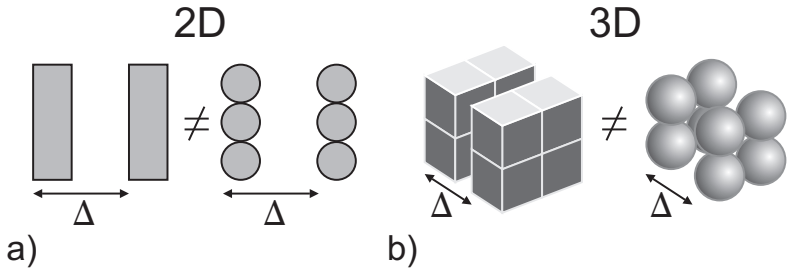

Figure 2.5: Schematic comparison of QPM structures with a) rectangular and circular motif in 2D and b) orthorhombic and spherical motif in 3D.

shown before, the highest normalized efficiency for an orthorhombic lattice with a spherical motif is 0.190, which is even smaller.

Basing on the data analysis, few conclusions can be made. First of all, amount of working material strongly influences on a value of the Fourier coefficient. This effect requires a close investigation in further subsection. Second, although 1D-like structures give the highest efficiency coefficients, they are limited with one direction. In contrast, the cubic lattice with spherical motifs has an efficiency smaller, by a factor of 2.5, but it is equal for three orthogonal directions. Third conclusion

is the presence of special aspects of an extension of 2D structures to 3D space, for example, by using cylindrical and spherical motif with different motif/periodic ratios (Figure 2.6).

Cylindrical motif is more complicated than spherical one. It has a symmetrical axis of rotation and it is important to decide its position referred to a lattice. Let us assume that the axis of rotation belongs to z-axis hence corresponding Fourier transform is calculated by:

$$S\left(\mathbf{K}\right) = \frac{2\pi hP}{V\sqrt{K_x^2 + K_y^2}}\text{sinc}\left(\frac{K_z h}{2\pi}\right) J_1\left(R\sqrt{K_x^2 + K_y^2}\right), \qquad (2.16)$$

where h is the cylinder height and $J_1\left(x\right)$ is a Bessel function of the first order. In particular cases when $\sqrt{K_x^2 + K_y^2} = 0$, we can use well-known limit $\lim_{x\to\infty} \frac{J_1(x)}{x} = \frac{1}{2}$.

2D structure in the Figure 2.6 can be a top view of different 3D structures. Calculations for this 2D structure suppose that it looks like 3D structure in Figure 2.6a, when $h/c = 1$. That's why they have similar Fourier coefficients for corresponding 2D orders. These coefficients are higher than that in other structures, but all other structures have more orders useful for QPM in all three dimensions.

The final conclusion of this subsection is that the spherical motif seems to be the only appropriate one for the formation of 3D QPM structures due to its symmetry. The next subsection will focus on the optimization of 3D QPM structures by investigating the nonlinear

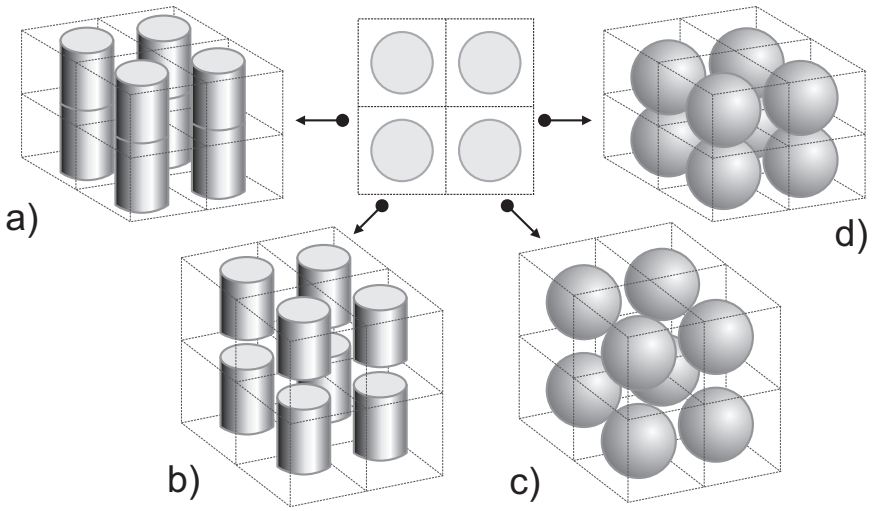

Figure 2.6: Extension of 2D structure to 3D space using cylindrical and spherical motifs, with different motif/period ratios.

coefficients as a function of spherical and cubic motifs, of the filling factor of the 3D QPM structures, and the propagation direction of the fundamental light beam.

2.4 Optimization of 3D QPM structures and filling factor

Previous subsections has already showed the highest values of Fourier coefficients for first orders of orthorhombic and spherical motifs in cases of orthorhombic and cubic lattices. However, more complicated structures might give higher conversion efficiency. For example, it is well known that in the case of photonic crystals, DC lattices possesses the best photonic bandgap [63]. Of course, QPM structure differs from

structure for photonic bandgaps, but here a few well-known complicated structures will be examined and their efficiency will be compared. To be more exact, simple cubic (SC) lattice with BCC, FCC and DC lattices will be compared using spherical motifs, which is the simplest symmetric motifs and also it is similar to real fabricating structures.

As it was mentioned before, complicated lattice is a combination of simple lattices. The simplest 3D structure is the SC structure. Reference [61] briefly describes basic principles of organization of such lattices like BCC, FCC and DC using method of shifted basis points. There can be two or more basis points. For example, the BCC lattice can be presented as two shifted SC lattices, the FCC lattice consists of four SC lattices, and the DC lattice is a set of two FCC lattices. Table 2.3 demonstrates formulas to calculate Fourier coefficients for BCC, FCC and DC lattices basing on SC lattice. Increasing in structure complicacy affects complicacy of overlapping conditions hence calculations only for cubic and spherical motifs are presented. They are symmetrical and provide simple analytical dependence of parameters. According to Table 2.3, for a cubic motif with a side size X the Fourier coefficients depend on parameter (X/a). For a spherical motif with a radius R the Fourier coefficients depend on parameter (R/a). Here a corresponds to the length of the primitive vector.

Due to the complicated configuration with shifted basic points, not all RLVs are available in the new lattices, hence they miss some orders. First orders for BCC lattice are $(1,1,0)$, $(2,0,0)$, $(2,1,1)$ and

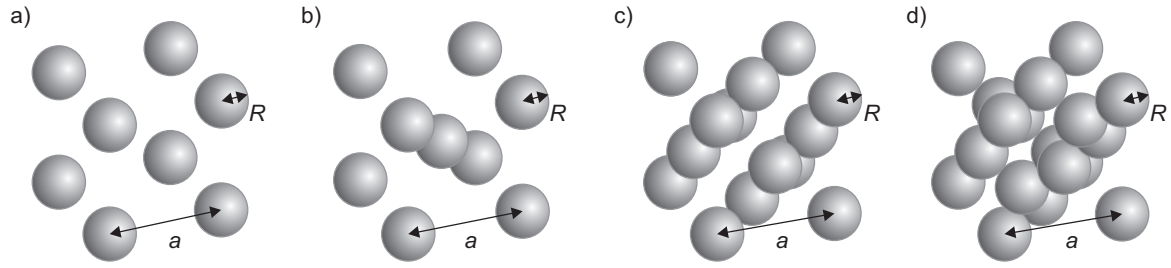

SC	
Order	$\|G\|^2$
(1,0,0)	0.0049
(1,1,0)	0.0033

BCC	
Order	$\|G\|^2$
(1,1,0)	0.0131
(2,0,0)	0.0053

FCC	
Order	$\|G\|^2$
(1,1,1)	0.0340
(2,0,0)	0.0241

DC	
Order	$\|G\|^2$
(1,1,1)	0.0680
(2,2,0)	0.0068

Figure 2.7: Four 3D structures with fixed ratio $R/a = \sqrt{3}/8$: a) SC, b) BCC, c) FCC, and d) DC. The tables present Fourier coefficients of first orders for each corresponding structure. Normalized efficiency is calculated for the "+/-"structure.

$(2, 2, 0)$. First orders for FCC lattice are $(1, 1, 1)$, $(2, 0, 0)$, $(2, 1, 0)$ and $(2, 2, 2)$. First orders for DC lattice are $(1, 1, 1)$, $(2, 2, 0)$, $(3, 1, 1)$and $(3, 3, 1)$. As far as it is symmetrical lattice, most of listed orders have coupled orders, which have equivalent values of Fourier coefficients, i.e. $|\mathbf{G}_{200}|^2 = |\mathbf{G}_{020}|^2 = |\mathbf{G}_{002}|^2$. That means that lattices provide many equivalent RLVs, i.e., many equivalent propagation directions.

Indeed, as mentioned previously, in the case of nonlinear optics, it requires a balance between the high symmetry of the QPM structures and the nonlinear material quantity. It seems that DC has both advantages, good symmetry and enough material quantity in a unit cell. This particular experiment which shows the influence of amount of materials on the value of the Fourier coefficient is illustrated in Figure 2.7. The ratio between radius of motif and QPM structure periodicity is fixed at a reasonable value, because of motif overlapping conditions. For DC lattice R/a ratio cannot exceed $\sqrt{3}/8$ (Table 2.3),

otherwise spheres will start to overlap each other. Fourier coefficient for this parameter in DC lattice is the highest, $|\mathbf{G}_{111}|^2 = 0.068$. Examining another lattice with $R/a = \sqrt{3}/8$, the highest possible coefficient slightly decreases, first in FCC lattice, then in BCC lattice and finally in SC lattice. Coefficient for the SC lattice, $|\mathbf{G}_{111}|^2 = 0.0049$, is more than 10 times smaller. This can be a reasonable proof how amount of working material and its ratio are important.

However, it does not prove that DC is the best structure. While DC lattice with spherical motifs is limited with ratio $R/a = \sqrt{3}/8$, SC lattice with spherical motifs is limited by $R/a = 0.5$. Here, the filling factor can be increased by increasing radius of spherical motif. Therefore the influence of the material filling factor on the nonlinear coefficients of a 3D QPM SC structure can be studied.

The dependence of Fourier coefficients of the SC lattice on the filling factor is presented in Figure 2.8 for a cubic motif and in Figure 2.9 for a spherical motif. In case of cubic motifs, a filling factor is used as X/a, where X is the side length of motifs and a is the length of SC lattice side. In case of spherical motifs with radius R, a ratio D/a is used. Here, D is equal to $2R$ to bring into accordance plots in Figure 2.9 and in Figure 2.8.

The most efficient order for the SC lattice in both cases is the first order $(1, 0, 0)$. The cubic motif shows the maximum efficient Fourier coefficient $|\mathbf{G}_{100}|^2 = 0.064$, at the point where $X/a = 0.73$. Next orders get maximum at point $X/a = 0.585$ where $|\mathbf{G}_{110}|^2 = 0.012$, and

Table 2.3: Fourier coefficients and limitations of motifs for SC, BCC, FCC and DC lattices for "+/-"structures.

Lattice types	Fourier coefficients
Simple cubic	For cubic motif: $\mathbf{G}_{sc} = 2\frac{X^3}{a^3}\text{sinc}\left(m\frac{X}{a}\right)\text{sinc}\left(n\frac{X}{a}\right)\text{sinc}\left(q\frac{X}{a}\right)$, $\frac{X}{a} \leq 1$ For spherical motif: $H = 2\pi\sqrt{m^2+n^2+q^2}$ $\mathbf{G}_{sc} = \frac{8\pi}{H^3}\left(\sin\left(H\frac{R}{a}\right) - H\frac{R}{a}\cos\left(H\frac{R}{a}\right)\right)$, $\frac{R}{a} \leq 0.5$
Body-centered cubic	$\mathbf{G}_{bcc} = \mathbf{G}_{sc}\left(1+\exp\left(i\pi\left(m+n+q\right)\right)\right)$, $\frac{X}{a} \leq 0.5$, $\frac{R}{a} \leq \frac{\sqrt{3}}{4}$
Face-centered cubic	$\mathbf{G}_{fcc} = \mathbf{G}_{sc}\left(1+\exp\left(i\pi\left(n+q\right)\right)+\exp\left(i\pi\left(m+q\right)\right)+\exp\left(i\pi\left(m+n\right)\right)\right)$, $\frac{X}{a} \leq 0.5$, $\frac{R}{a} \leq \frac{\sqrt{2}}{4}$
Diamond cubic	$\mathbf{G}_{dc} = \mathbf{G}_{fcc}\left(1+\exp\left(i\pi\left(m+n+q\right)/2\right)\right)$, $\frac{X}{a} \leq 0.25$, $\frac{R}{a} \leq \frac{\sqrt{3}}{8}$

at point $X/a = 0.5$ where $|\mathbf{G}_{111}|^2 = 0.004$. The spherical motif shows the maximum efficient Fourier coefficient for the first order ($|\mathbf{G}_{100}|^2 = 0.101$) and for the third order ($|\mathbf{G}_{111}|^2 = 0.007$), when $D/a = 1$. The second order in this case shows its maximum $|\mathbf{G}_{110}|^2 = 0.0126$ at ratio $D/a = 0.353$.

Obviously, the spherical motif has higher efficient Fourier coefficients in SC lattice than the coefficient obtained with a DC structure. Again the spherical motif in a cubic lattice showed itself as the best configuration for 3D QPM structures. It is also a perspective in the sense that the first and the third QPM orders require the same configuration to provide the highest coefficient. Even if the third order is noncomparable smaller than the first order.

Table 2.4 displays the most efficient orders with the highest Fourier coefficients demonstrated by SC, BCC, FCC and DC lattices. It is worth mentioning that the spherical motif provides better nonlinear coefficients in comparison with those obtained by the cubic motif. The most convincing reason is a high symmetry of the spherical motif. These results are interesting and attractive, because the spherical motif in a cubic lattice is very close to what can be realized in practice. That reduces challenges of fabrication requirements, and the 3D QPM structures can be realized in polymer material doped with nonlinear particles.

One more important aspect of our calculations and optimizations can be noted as reversibility. For example, the motifs always have

Table 2.4: Optimum Fourier coefficients of SC, BCC, FCC, and DC lattices for "+/–"QPM structures, made by two particular motifs.

Order	Cubic motif		Spherical motif	
	$\lvert\mathbf{G}_{\max}\rvert^2$	X/a	$\lvert\mathbf{G}_{\max}\rvert^2$	R/a
Simple cubic				
$(1,1,0)$	0.064	0.730	0.101	0.500
$(2,0,0)$	0.012	0.585	0.013	0.353
Body-centered cubic				
$(1,1,0)$	0.041	0.500	0.050	0.352
$(2,0,0)$	0.004	0.365	0.012	0.433
Face-centered cubic				
$(1,1,1)$	0.066	0.500	0.060	0.289
$(2,0,0)$	0.016	0.365	0.025	0.247
Diamond cubic				
$(1,1,1)$	0.016	0.500	0.068	0.216
$(2,2,0)$	0.010	0.500	0.012	0.177

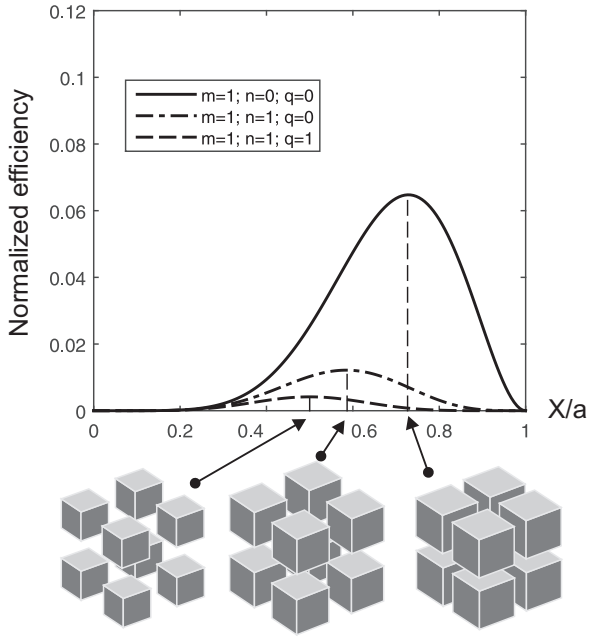

Figure 2.8: Normalized efficiency of SC lattice for the three first orders $(1,0,0)$, $(1,1,0)$, and $(1,1,1)$ as a function of ratio between the size of cubic motif, X, and the lattice periodicity, a. Normalized efficiency is calculated for the "+/–"structure.

$\chi^{(2)} = +1$, while surrounding material is assigned a value $\chi^{(2)} = -1$ or $\chi^{(2)} = 0$. The case of "+/-"QPM structures will not show any difference if signs are reversed to "-/+"QPM structure. However, in case of "+/0"and "0/+"3D QPM structures, the result can differ due to the material with $\chi^{(2)} = 0$. Let define that the "block motif"possesses $\chi^{(2)} = +1$ while surrounding medium possesses $\chi^{(2)} = 0$. The "hollow motif"presents the opposite situation, which can be called "0/+"QPM structure. Using the linearity of the Fourier transform, it can find out that $G_{block} = -G_{hollow}$ and hence $|\mathbf{G}_{block}|^2 = |\mathbf{G}_{hollow}|^2$.

Figure 2.10 shows the variation of the nonlinear coefficients as a function of filling factor. The filling factor is calculated as $V_{nonlinear\ material}/$

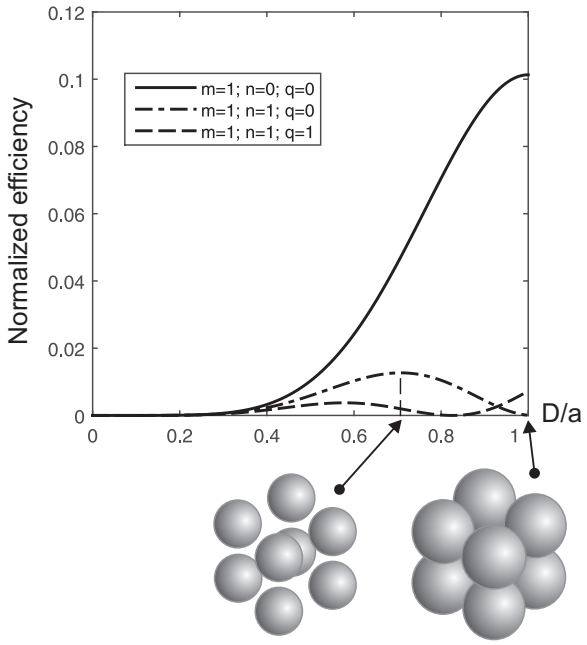

Figure 2.9: Normalized efficiency of SC lattice for three first orders $(1,0,0)$, $(1,1,0)$, and $(1,1,1)$ as a function of ratio between the spherical motif diameter, D, and the lattice periodicity, a. Normalized efficiency is calculated for the "+/–"structure.

$V_{unitcell}$. A cubic lattice with cubic motifs assumes that length of side of unit sell is $a = 1$. The length of motif side X increases from 0 to 1. When the filling factor is equal to 1, there is only nonlinear material, while $V_{nonlinear\ material}/V_{unitcell} = 0$, there is no any active material for SHG. Solid line and dashed line present nonlinear coefficients for block motif and hollow motif, respectively. For the case of the first order $(1,0,0)$, a crossing of curves is obtained when filling factor is equal to 0.5 while the motif side is equal to 0.793.

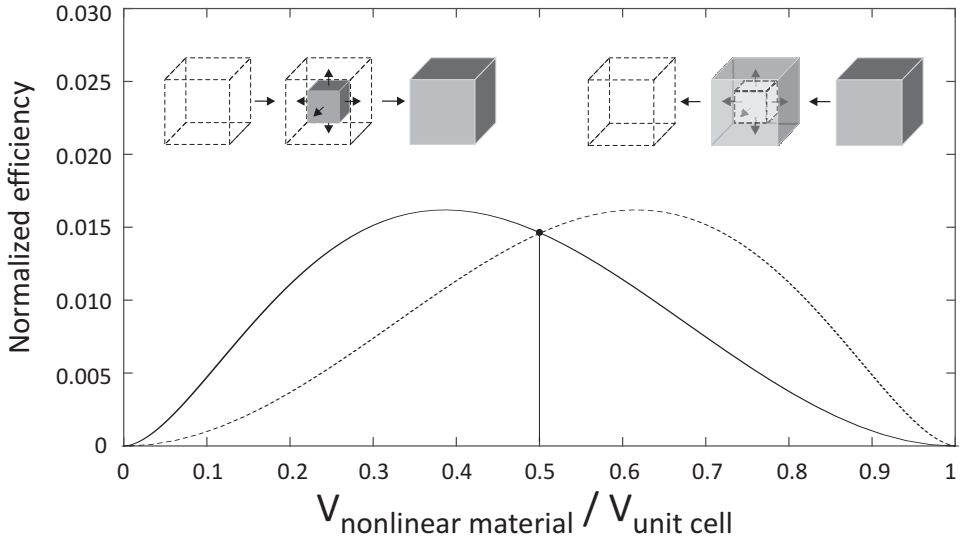

Figure 2.10: Normalized efficiency for $(1, 0, 0)$ order of a SC lattice with a cubic motif. The solid and dashed lines represent efficiency curves of 3D QPM structures made by solid and hollow motifs, respectively. The insert shows the evolution from null to full material (block motif) and from full material to null material (hollow motif).

2.5 Real structure approach

Doubtless that real motifs are more complicated than spheres or cubes. Their possible shape strongly depends on the nonlinear materials and fabrication techniques. Taking into account of these aspects, one of the frequently used methods for fabrication of QPM structures in polymers is optical lithography.

The Reference [64] conclusively presents the fabrication of 3D templates with $\chi^{(2)} = 0$ by the interference technique, which has certain advantages like large-area, fabrication control, uniformity and time saving. The thickness of 3D samples can be desirable in case of a holographic assembly technique [65] or can achieve 300 μm by using

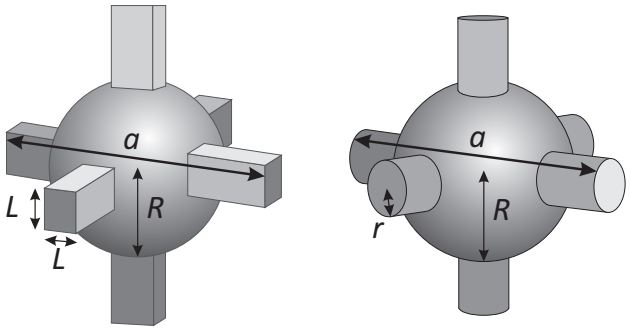

Figure 2.11: Two motifs with connections: (a) "square-cut"and (b) "circular-cut". a is the lattice period and R is the radius of spherical motif located in the center of the unit cell. Each motif has 6 symmetrical connections where the square cross-section has a length of L and the sphere cross-section has a radius r.

an ultra-low absorption method [66]. It is important to note that this fabrication technique proposes to fill in voids of 3D templates with nonlinear material $\chi^{(2)} = +1$, resulting in a "+/0"QPM 3D structure. It is necessary that polymer template with $\chi^{(2)} = 0$ and injected nonlinear material with $\chi^{(2)} \neq 0$ should have the same refractive indices or these values should be very close to each other, to avoid losses of fundamental and second harmonic signals due to the reflection at each interface.

Advanced motifs were modeled using illustrations of really fabricated templates. Aiming to achieve balanced structure like in Figure 2.9 where $D/a = 1$, a model, which consists of sphere-like main motifs connected to each other by small connections, is required (Figure 2.11). Calculations were limited by taking into considerations only SC lattice. According to "real structure approach", two types of connections were modeled, "square-cut"and "circular-cut".

Both motifs in Figure 2.11 have several common parameters: a is a length of the cubic lattice unit cell or it can be called a repetition period in x, y and z direction, R is a radius of the main motif. According to the name, the cross section of "square-cut"connection has a square shape with a side length L. The cross section of "circular-cut"connection has a radius r. For calculations, the main spherical motif is introduced with $\chi^{(2)} = +1$ in the center of the SC lattice. Each motif has six symmetrical connections with $\chi^{(2)} = +1$. It should be mentioned that the size of the connection is rather small in comparison with the main motif. This assumption allows us to simplify the form of connection hence the "square-cut"connection is presented as an orthorhombic form and the "circular-cut"connection becomes a cylinder. Due to the property of linearity of the Fourier transform, the Fourier coefficients can be calculated for these two complicated motifs, as shown in Table 2.5. Here the Fourier transform of the cylindrical motif also appears as Bessel functions and hence Table 2.5 shows specific cases for calculation.

Figure 2.12 represents the surface of normalized Fourier coefficients for "+/0"type structures, i.e., SC lattice, spherical motif and "square-cut"connections. Coefficients were calculated for the highest $(1, 0, 0)$ order. Several limits were put on ratios, for example $L/a \leq 0.1$, because connections are assumed to be small and $L/a < R/a$ due to the same reason. Plot in Figure 2.12 has also axis limit $0.3 \leq R/a \leq 0.5$. This limit allows to pay attention to the area with the highest coef-

Table 2.5: Fourier coefficients for two types of complicate motif with connections: spherical motif with square-cut connections and with circular-cut connections

Motif	Fourier coefficients
Spherical motif	$H = 2\pi\sqrt{m^2+n^2+q^2}$
with square-cut	$\mathbf{G}_{mnq} = \frac{4\pi}{H^3}\left(\sin\left(H\frac{R}{a}\right) - H\frac{R}{a}\cos\left(H\frac{R}{a}\right)\right) + \frac{L^2}{a^2}\mathrm{sinc}\left(n\frac{L}{a}\right)\mathrm{sinc}\left(q\frac{L}{a}\right)\left(\mathrm{sinc}\left(m\right) - 2\frac{R}{a}\mathrm{sinc}\left(2m\frac{R}{a}\right)\right)$
connections	$+\frac{L^2}{a^2}\mathrm{sinc}\left(m\frac{L}{a}\right)\mathrm{sinc}\left(q\frac{L}{a}\right)\left(\mathrm{sinc}\left(n\right) - 2\frac{R}{a}\mathrm{sinc}\left(2n\frac{R}{a}\right)\right)$
	$+\frac{L^2}{a^2}\mathrm{sinc}\left(m\frac{L}{a}\right)\mathrm{sinc}\left(n\frac{L}{a}\right)\left(\mathrm{sinc}\left(q\right) - 2\frac{R}{a}\mathrm{sinc}\left(2q\frac{R}{a}\right)\right)$
Spherical motif	$H = 2\pi\sqrt{m^2+n^2+q^2}$
with circular-cut	$\mathbf{G}_{mnq} = \frac{4\pi}{H^3}\left(\sin\left(H\frac{R}{a}\right) - H\frac{R}{a}\cos\left(H\frac{R}{a}\right)\right) + \frac{r}{a}\frac{1}{\sqrt{n^2+q^2}}J_1\left(2\pi\frac{r}{a}\sqrt{n^2+q^2}\right)\left(\mathrm{sinc}\left(m\right) - 2\frac{R}{a}\mathrm{sinc}\left(2m\frac{R}{a}\right)\right)$
connections	$+\frac{r}{a}\frac{1}{\sqrt{m^2+q^2}}J_1\left(2\pi\frac{r}{a}\sqrt{m^2+q^2}\right)\left(\mathrm{sinc}\left(n\right) - 2\frac{R}{a}\mathrm{sinc}\left(2n\frac{R}{a}\right)\right)$
	$+\frac{r}{a}\frac{1}{\sqrt{m^2+n^2}}J_1\left(2\pi\frac{r}{a}\sqrt{m^2+n^2}\right)\left(\mathrm{sinc}\left(q\right) - 2\frac{R}{a}\mathrm{sinc}\left(2q\frac{R}{a}\right)\right)$
	In particular case $\sqrt{n^2+q^2} = 0$:
	$\frac{r}{a}\frac{1}{\sqrt{n^2+q^2}}J_1\left(2\pi\frac{r}{a}\sqrt{n^2+q^2}\right) = \pi\frac{r^2}{a^2}$

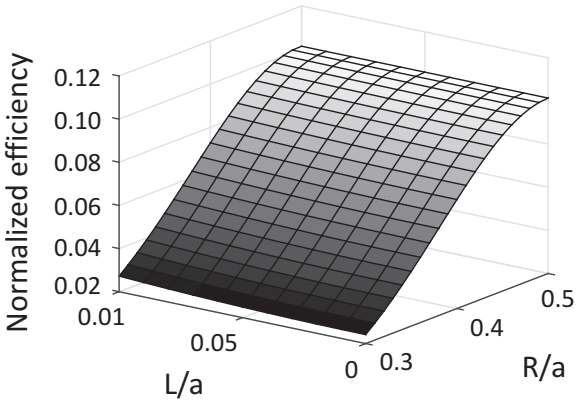

Figure 2.12: Surface of normalized efficiency of spherical motifs with orthorhombic connections as a function of $L/a \leq 0.1$ and $0.3 \leq R/a \leq 0.5$. Normalized efficiency is calculated for $(1, 0, 0)$ order for "+/-"structure.

ficients. If $L/a = 0$ the structure is the same as in Figure 2.9 when there are no connections. Plot vividly demonstrates that appearance of connections does not strongly influence on normalized efficiency.

Figure 2.13 presents similar behavior for "circular-cut"connections. Essential limits are $r/a \leq 0.1$ and $0.3 \leq R/a \leq 0.5$. A slight increase of the nonlinear coefficient appears as a function of the r/a. Of course it is negligible and can be explained by the small increase of the quantity of the nonlinear material. That means that the influence of this connection on the final results is of little importance, and this motif can be treated as spherical motifs in the SC lattice.

2.6 Conclusion

This chapter presented a theoretical model of 3D QPM structures and analyzed QPM conversion efficiency of SHG in periodic 3D nonlinear

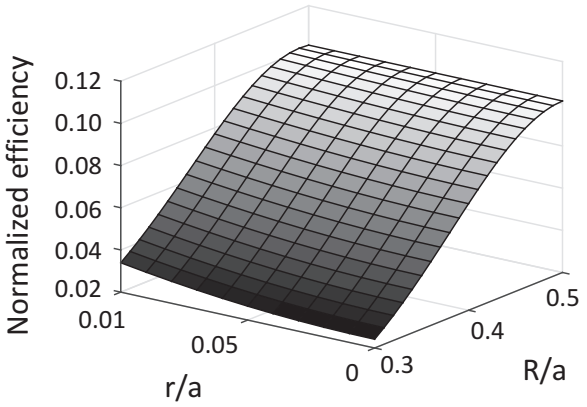

Figure 2.13: Surface of normalized efficiency of spherical motifs with cylindrical connections as a function of $r/a \leq 0.1$ and $0.3 \leq R/a \leq 0.5$. Normalized efficiency is calculated for $(1, 0, 0)$ order for "+/-"structure.

structures with various lattices, shapes and parameters of motifs. It demonstrated a general formula for calculations of QPM efficiency for basic Bravais lattices (triclinic, orthorhombic, cubic and hexagonal) and for simplest motifs (orthorhombic, cubic, spherical and cylindrical). General data displayed in Table 2.2 and Table 2.3 can be used to calculate Fourier coefficients of any QPM order for particular lattices and motifs.

It can be noted that generalization is applicable to 1D and 2D QPM structures reported in previous papers, because these structures are particular cases of 3D QPM structures. It demonstrates a good agreement with previously published results.

It was found out that the conversion efficiency of the 3D QPM structures is weaker than that of the 2D QPM. The reason of this dependence is the quantity of the nonlinear material. However, the 3D QPM structure has an obvious advantage. It has much more QPM

orders than 1D and 2D structures; hence it enhances the flexibility of the RLV design and enables more complicated nonlinear processes in the same 3D structure.

According to investigation, the most promising combination of lattices and motifs turned out to be a cubic lattice with spherical motifs. This structure showed the highest nonlinear coefficients for the first orders. It seems that high symmetry of spherical motifs provides the best filling factor for the highest efficiency coefficients.

It is also demonstrated that it is easier to fabricate 3D periodical structures with the cubic lattice and with motif shapes like spheres. These sphere-like motifs will be connected by small connectors. That is the reason why the motif was modified and small connections were added. However they didn't bring any noticeable changes in QPM efficiency. In conclusion, among all structures, the cubic lattice with spherical motifs is the most prospective for fabrication to approve 3D QPM.

Chapter 3

Experimental realization of 3D QPM structures

3.1 Schemes of fabrication using interference techniques

This chapter is devoted to investigation of materials to find an appropriate one for fabrication of 3D QPM structures by the interference technique, which provides uniform result upon a large area in a short time. Two possible schemes are investigated.

The first scheme presented in Figure 3.1 proposes first to synthesize DAST nanocrystals in polymer (or monomer) matrix and then

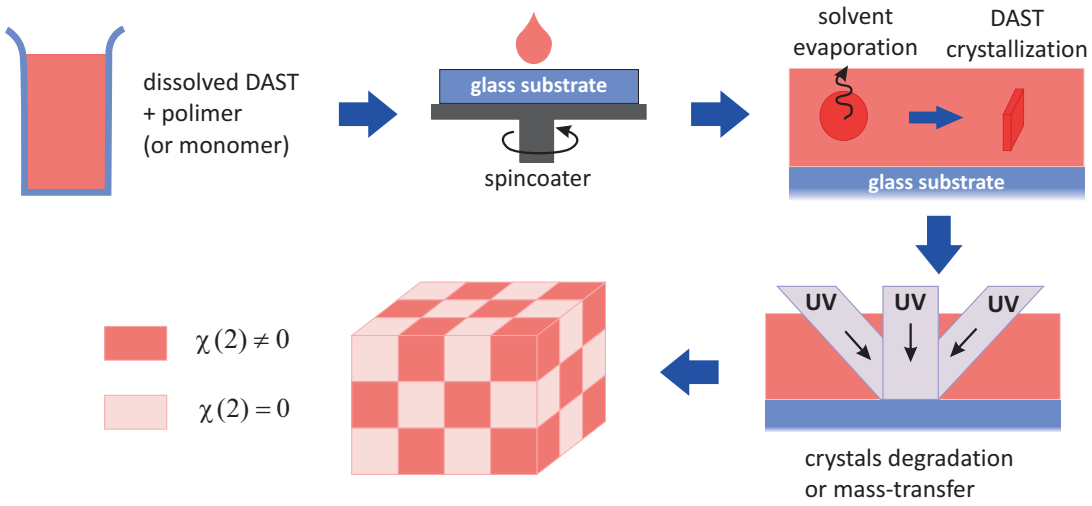

Figure 3.1: Fabrication process of 3D QPM structure by the interference technique.

pattering them by using the interference technique. The interference technique can cause mass-transfer effect in polymerizing monomers, and locally heating the samples making DAST crystals transform into amorphous form.

The second scheme presented in Figure 3.2 proposes to fabricate templates using the interference technique and SU-8 photoresist. Then filling template voids by solution containing dissolved DAST leads to possibility to synthesize DAST nanocrystals inside these voids and hence achieve a spatial distribution of nonlinear materials.

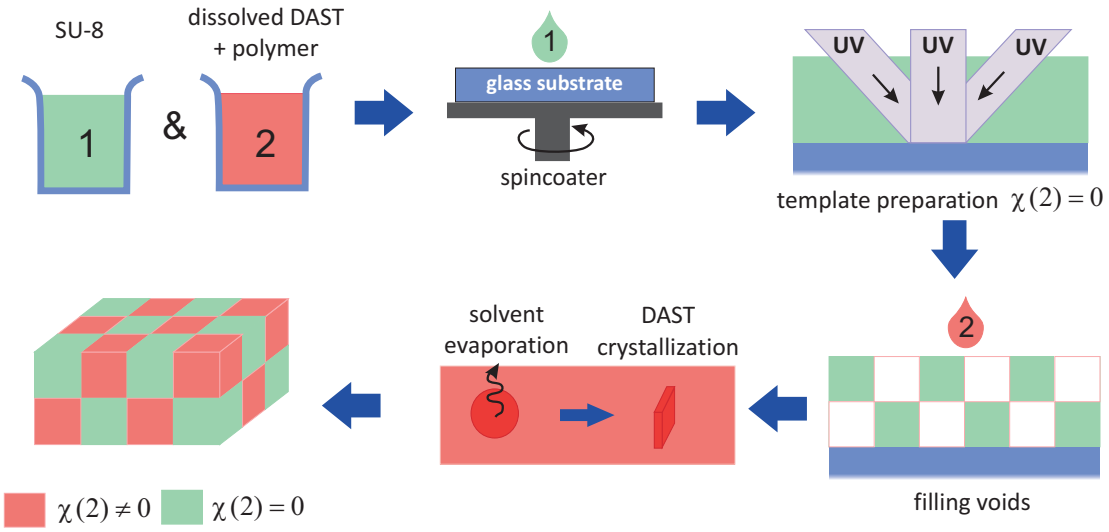

Figure 3.2: Fabrication process of 3D QPM structure by template preparation and filling voids with nonlinear material.

3.2 Synthesis of DAST submicron crystals with controllable size

First of all, parameters of DAST crystallization were investigated in order to find out conditions which influence on the size, shape and optical parameters of DAST crystals. Poly(methyl methacrylate) (PMMA) was demonstrated as an excellent host material as reported in previous works [59, 60], hence it was used as a polymer matrix for embedding DAST crystals. Also to create polymerizable nanocomposite with embedded DAST crystals, several monomers were tested as host materials. Two monomers, isodecyl acrylate (IDA) and trimethylolpropane ethoxylate (1 EO/OH) methyl ether diacrylate (TMP), showed weak chemical interaction with DAST crystals and good properties com-

plementation with each other. Hence this mixture can be used as a base for polymerizable nanocomposite. This section is divided into two subsections in order to analyze two synthesized materials.

3.2.1 Synthesis of DAST submicron crystals in PMMA

In this subsection, PMMA (Plexiglas® V045) was dissolved in chloroform (CL0218 Scharlau) and DAST (CAS:80969-52-4 Genolite biotek) was dissolved in methanol (322415 Aldrich). Methanol was used as a solvent because it is mentioned as a good solvent for DAST in several References [52, 53, 55]. However methanol has miscibility with water, hence it should be protected from water in the air by well sealed lid. Chloroform was chosen as a solvent for PMMA because of its boiling point (61.2°C) which is very close to the boiling point of methanol (64.7°C). That can provide common speed of solvents evaporation.

The DAST mass in all solutions was equal to 2% of the PMMA mass, because it was the optimum amount to avoid uncontrollable growth of big crystals. The amount of methanol was calculated from the solubility limit of DAST in methanol at room temperature [67]. In order to investigate the influence of the film thickness on the synthesis of DAST crystals, the concentration of PMMA in chloroform was changed hence viscosity of solutions also differed. Six solutions with 1, 3, 5, 8, 10, and 15% of DAST + PMMA in chloroform were prepared.

Figure 3.3a presents the preparation process of DAST+PMMA so-

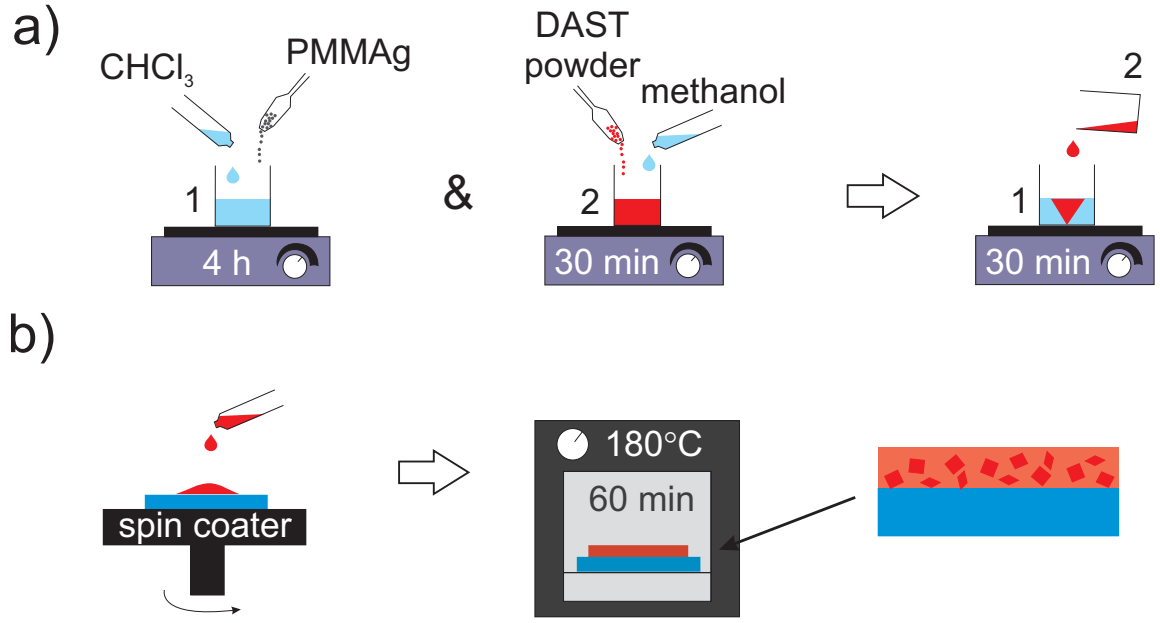

Figure 3.3: a) preparation of DAST+PMMA solution and b) fabrication of thin film containing DAST crystals.

lution. First, PMMA was dissolved in chloroform and DAST was dissolved in methanol. Dissolved DAST was added into PMMA solution and was stirred together to achieve homogeneity. Figure 3.3b presents the fabrication of thin film containing DAST crystals. The films were formed by two-step centrifuging (100 and then 1500 rpm for 10 s). Annealing was performed at 180°C with different durations due to different thicknesses of samples (see Table 3.1).

The method described in [8] is based on molecular crystals aggregation, upon which the size of particles is limited by the transport of materials through the viscous polymer solution. The formation of the film and particles in the mixture starts with centrifuging when solvent evaporation occurs with identical rates and terminates after

complete evaporation of the solvent during annealing. Fast removal of the solvent (in a few milliseconds) during spincoating of the polymer film provokes conditions for phase separation. One phase forms microbubbles of a DAST solution in methanol while the second phase contains the PMMA solution in chloroform. Following fast evaporation of methanol leads to the formation of a submicron DAST crystals in each bubble. After complete escape of solvents, a PMMA matrix with embedded submicron DAST particles can be observed. These particles have an amorphous structure, but transforms into a crystal structure during thermal treatment [60].

Figure 3.20 shows the SEM (scanning electron microscope) images of samples on identical scales (scale division of 10 μm). The samples were prepared as follows: the films on a substrate were immersed in toluene (34929 Riedel-de Haen). It dissolved the top of PMMA layer. At the same time, the DAST crystals were not damaged and remained on the substrate, because toluene does not dissolve DAST crystals. The only drawback of toluene is that it absorbs water from the air; hence it can't be used for a long time and should be sealed with lid otherwise crystals will be dissolved. Then, the samples were coated with a thin ($\sim$7 nm) gold layer and photographed with an SEM (Hitachi S-3400N). The sizes of crystals were measured from the SEM images and presented in the Table 3.1. It is obvious that the film thickness affects the speed rate of solvents evaporation. Evaporation of thicker films is more complicated and causes merging of bubbles hence crystals

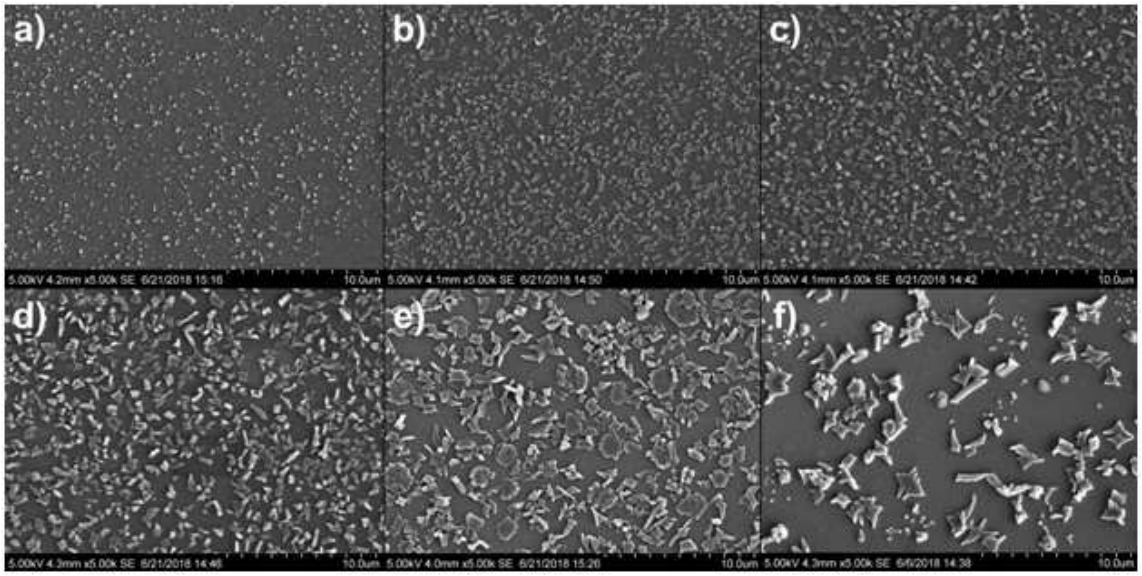

Figure 3.4: SEM images of samples prepared from solutions with concentrations of (a) 1, (b) 3, (c) 5, (d) 8, (e) 10, and (f) 15%.

grow larger and with bigger variety of forms. It is worth mentioning that some regions of the samples prepared from a solution with a concentration of 15% contained large plane crystals of a complex shape, which, probably, were formed due to the diffusion of methanol bubbles with DAST along the substrate under the solid PMMA film.

The absorption spectra before and after annealing were measured using a PerkinElmer Lambda 950 UV/VIS spectrophotometer and are shown in the Figure 3.5 The appearance of the pick near 550 nm in spectra after annealing is a fingerprint of the green-red nonlinear crystalline form of DAST[68]. After annealing, the films became more transparent and pinkish which is also a sign of nonlinear crystalline form. Table 3.1 shows absorption coefficient after annealing. Values are not normalized and take into consideration thickness of the sample.

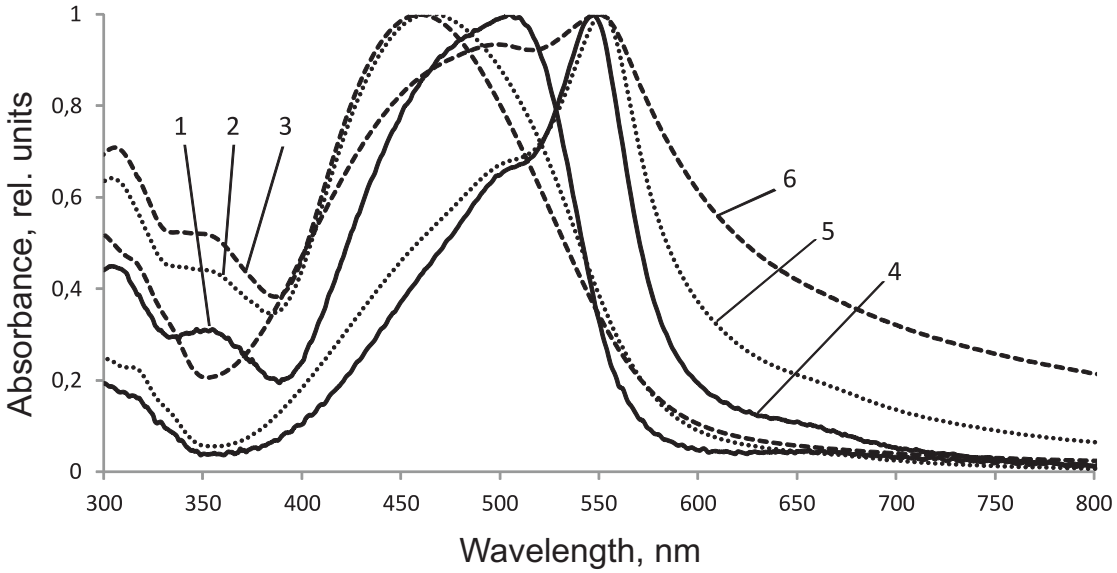

Figure 3.5: Absorption spectra measured (1–3) before and (4–6) after annealing for samples prepared from solutions with concentrations of 1% (1, 4, solid curves), 5% (2, 5, dotted lines), and 15% (3, 6, dashed curves).

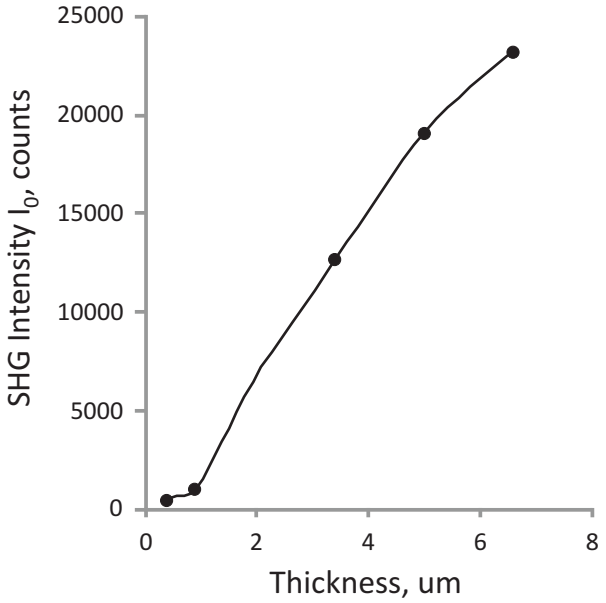

Figure 3.6: Dependence of SHG intensity (before absorption) on thickness of a sample.

Table 3.1 also presents SHG intensity which was measured using a CryLas FDSS laser with a wavelength of 1064 nm and an Ocean Optics USB2000+ spectrometer. The SH wavelength (532 nm) locates close to the peak of the DAST absorption spectrum hence there is an absorption of SHG signal by all samples. To find the initial SHG (before absorption) the Beer–Lambert law can be used:

$$I\left(l\right) = I_0 exp\left(-k_\lambda l\right), \tag{3.1}$$

where $I\left(l\right)$ is intensity of light that has passed the layer of substance with thickness l, I_0 is intensity at the entrance to the substance, k_λ is absorption coefficient.

Table 3.1 has absorption coefficient which is equal to $k_\lambda l$, because it takes into consideration thickness of samples. Hence table presents SHG intensity before it was partially absorbed. Figure 3.6 demonstrates linear dependence of SHG intensity on thickness of a sample, however size of DAST crystals differs in films from 70 to 2500 nm. This plot proves that size of crystals doesn't influence on SHG intensity.

In conclusion, the synthesis of DAST crystals can be controlled by different parameters, especially by viscosity of solution. The crystals in films deposited from solutions with concentrations of 1, 3, and 5% are plane and have an approximately rhombic shape, which is well known as classical green-red configuration of DAST crystals (see Figure 1.4b). The crystals in the 5% sample are very similar to the crystals obtained

Table 3.1: Comparative characteristics of samples with different concentrations of components in initial solutions.

Initial solution concentration, %	Film thickness, μm	Annealing time, min	Particle size, nm	Absorption coefficient	SHG intensity (after absorption), counts	SHG intensity (before absorption), counts
1%	0.4	10	70-150	0.061	416.20	442.38
3%	0.9	15	150-250	0.229	800.46	1006.45
5%	1.9	30	250-400	0.354	4456.38	6349.25
8%	3.4	45	250-1000	0.361	8791.05	12613.08
10%	5.0	80	250-1500	0.373	13107.00	19032.47
15%	6.6	90	250-2500	0.457	14672.82	23173.21

in [69]. Therefore, this solution is the most appropriate for the further experiments with filling voids in SU-8 template and examining bleaching capability. Average crystals size is 300 nm.

3.2.2 Synthesis of DAST submicron crystals in monomers

This subsection examines polymerizable nanocomposite. First it focused on solubility of DAST crystals in different monomers to find those which do not react with crystals. As expected, IDA (408956 Aldrich) does not chemically interact with DAST crystals, however this monomer is slowly polymerized. Also, the quality of the film is

very poor, because IDA forms a gummy material. This was the cause of decision to add another monomer to improve properties of polymerizable nanocomposite. However other monomers dissolved part of DAST crystals. TMP (415871 Aldrich) monomer showed the most poor chemical reaction with DAST powder, hence TMP was added to IDA as a supporting monomer.

The thin film of high quality requires an estimation of the best proportion of two monomers to obtain and to reach the best conditions for crystals formation. If the percentage of IDA is less than 30%, then the film became gummy. In the opposite, if the percentage of IDA excides 60%, then the film lost its homogeneity and deteriorated. In order to investigate properties of the thin film, three solutions with different IDA : TMP ratios were prepared. Chosen ratios were 3:7, 4:6 and 5:5.

DAST powder (CAS: 80969-52-4 Genolite biotek) has been separately dissolved in methanol (322415 Aldrich) corresponding to a solubility limit [67]. For all solutions, DAST amounted to 0.5% of IDA+TMP mixture. To start polymerization reaction, colorless monomers require an initiator and for this purpose In2 (2,2-Dimethoxy-2-phenyl-acetophenone, 196118 Aldrich) was added. Its amount equaled to 0.2% of monomers mixture.

Figure 3.7a presents a mixing order for preparation of DAST+monomers solution. First monomers were mixed to achieve a homogeneity, and separately, DAST was dissolved in methanol. Then DAST was

added into monomers and stirring together. Figure 3.7b presents the fabrication of thin films containing DAST crystals. Firstly, the solution was deposited on a glass substrate by Spin-Coater KW-4A centrifuge (Chemat Technology Inc.). The spincoating rate was adjusted to get the samples with a thickness equal 3 μm. An evaporation of methanol during spincoating initiated crystallization of DAST from solution as well as in case with PMMA. Secondly, the polymerization of a thin film proceeded under a mercury lamp in vacuum within 15 minutes and fixed DAST particles in the matrix. Thirdly, annealing process stimulates solvent evaporation and crystal growth. It is also important to complete cross-linking. Thin films were annealed at different temperatures (from 50°C to 140°C) and during different times (from 3 minutes to 45 hours) to determine the best combination. Starting point of film degradation was observed at 110°C. The experiment also showed that the appropriate annealing temperature is 80°C, and the suitable time of annealing is around 1.5 hours.

The UV-Vis absorption spectra were obtained by a Perkin-Elmer spectrophotometer 555. Measuring of the absorption spectrum is an important method to examine growth of DAST crystals. In Figure 3.8a the presence of narrow red-shifted band around 550 nm can be clearly observed. This is the fingerprint of acentric crystals of DAST green-red crystalline form which has efficiently high nonlinear properties [53]. Internal charge transfer broad band of DAST is centered at 490 nm. An additional method is a visual analysis via optical microscope. The

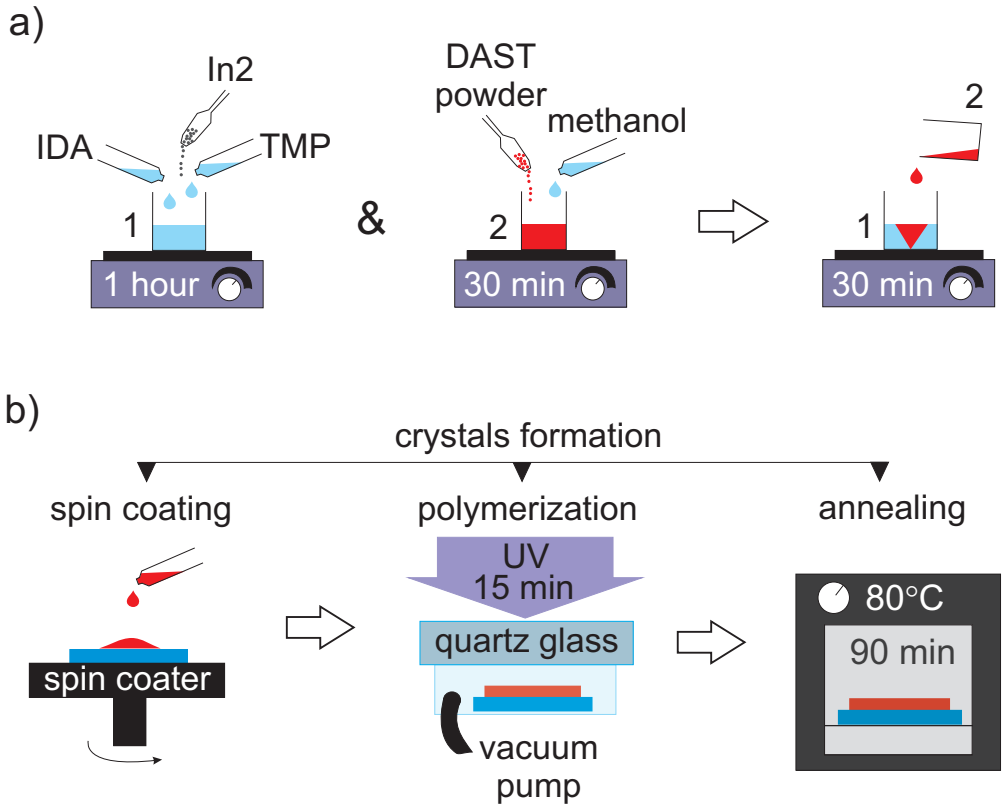

Figure 3.7: a) Preparation of DAST+monomers solution and b) fabrication of polymerized thin film containing DAST crystals.

samples were examined on the optical microscopes OLYMPUS STM6 and Nikon Eclipse Ci-S. Figure 3.8b-d shows microscope images. It is well seen decreasing of crystals size while amount of IDA in solution is increasing.

The examination of fluorescence and SH signals was provided by a modified low one-photon absorption direct laser writing (LOPA-DLW) setup [66] which is presented in Figure 3.9. This setup contains two lasers. A continuous-wave 532-nm laser (Oxxius frequency-doubled Nd-YAG laser) can be used for fluorescence excitation due to the fact

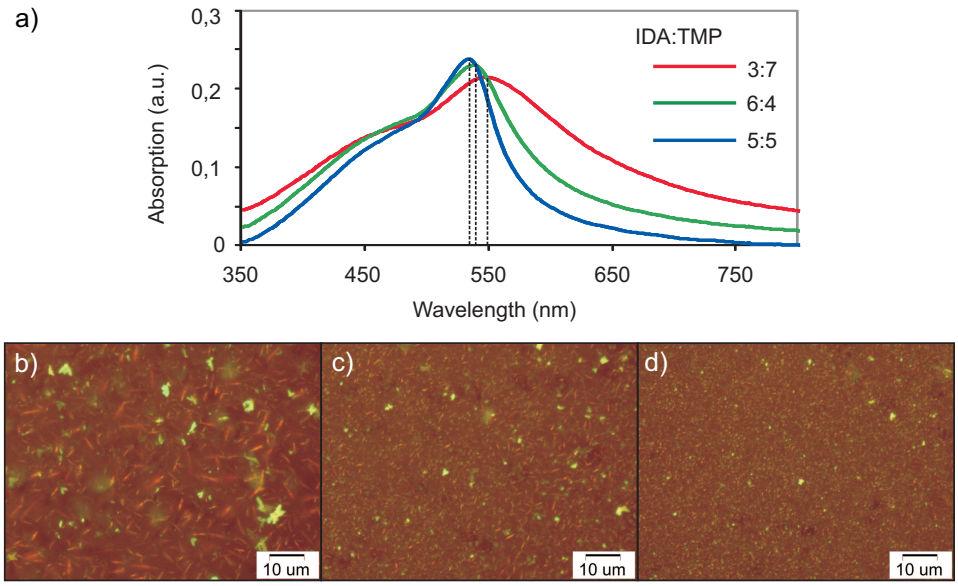

Figure 3.8: a) Absorption spectrum of thin films with DAST crystals fixed in polymerized matrix, which differs by ratio of two monomers. Microscope images of samples showing the variation of DAST crystals sizes as a function of monomers ratio: b) IDA : TMP = 3:7; c) IDA : TMP = 4:6; d) IDA : TMP = 5:5.

that 532 nm belongs to the peak absorption spectrum of DAST crystals. This laser possesses the following parameters: maximum power: 300 mW, coherence length: 300 m; pointing stability: 0.005 mrad/C. A pulsed 1064-nm laser (JDSU) has been used for SHG. This laser possesses the following parameters: maximum averaged power: 80 mW; pulse duration: 1 ns, repetition rate: 24.5 kHz. Both lasers integrated into the same setup and well-collimated to direct to the same sample area via a microscope objective. However flip-flop, mirror is required to switch from one laser to the other. A half-wave plate and a polarizer are used to adjust the laser power. The signal is detected by the APD (SPCM-AQRH-13 Perkin Elmer). Filters assure which wavelength signal was detected by the APD. Another flip-flop mirror can send the

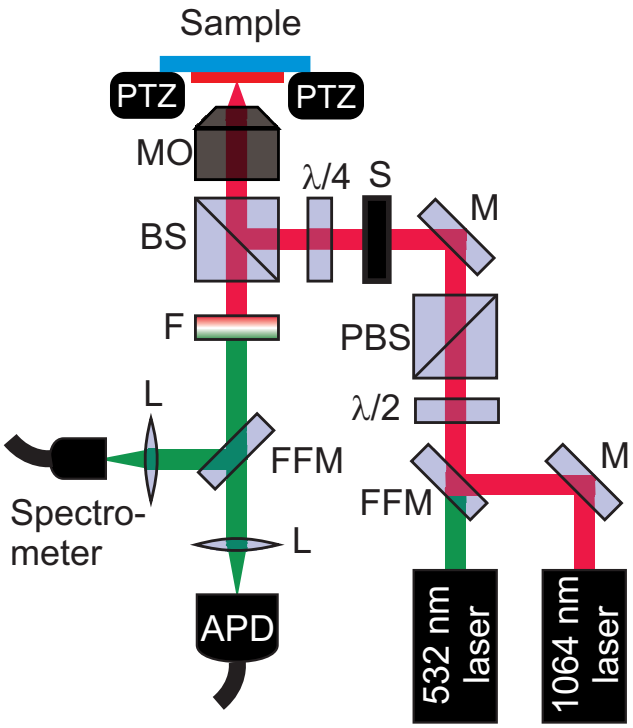

Figure 3.9: LOPA DLW setup. PZT: piezoelectric translator, MO: microscope objective, $\lambda/4$: quarter-wave plate, $\lambda/2$: half-wave plate, BS: beam splitter, PBS: polarizer beam splitter, M: mirror, FFM: flip-flop mirror, S: electronic shutter, L: lens, F: infrared filter, APD: avalanche photodiode.

emitted signal into the UV-vis spectrometer to check its spectrum.

The optical microscope image of DAST crystals embedded thin film is shown in Figure 3.10a. Figure 3.10b and Figure 3.10c present fluorescence mapping image and SH mapping image, respectively. Figure 3.10d presents a zoom in picture of SH mapping which suggests that crystals size is $\sim$1 μm and bigger. To measure the fluorescence spectrum, samples were excited by 532-nm laser. The excitation spectrum was blocked by a 580-nm long-pass filter. Figure 3.9e shows the fluorescence spectrum. A 1064-nm laser excited the sample to generate

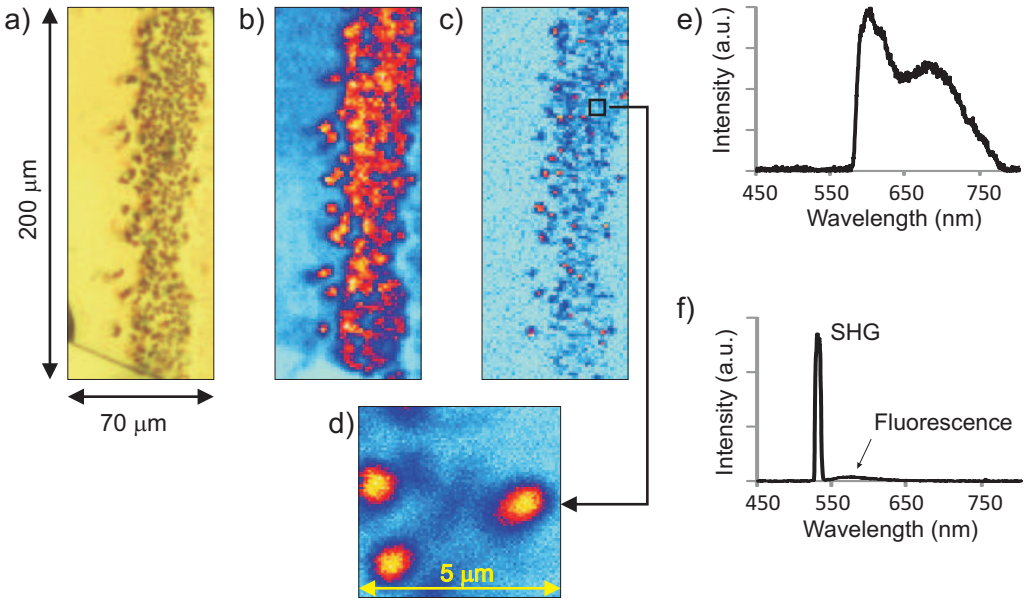

Figure 3.10: a) Optical microscope image of the sample; b) fluorescence mapping image obtained by scanning with a 532-nm laser of corresponding sample; c) SHG mapping image obtained by scanning with a pulsed 1064-nm laser; (d) zoom in of SHG mapping image with well-defined nonlinear crystals. e) Fluorescence spectrum obtained by excitation at 532 nm and f) SH spectrum obtained by excitation at 1064 nm.

SH spectrum which is shown in Figure 3.10f. Narrow, but strong peak appears at 532 nm. Additionally, the weak wide band was detected. It is red-shifted with respect to SH signal. Two mechanisms can explain this wide band signal: the first mechanism is one-photon absorption induced by SH signal at 532 nm, the second mechanism is two-photon absorption due to pulsed excitation at 1064 nm. The first mechanism is more expectable because two-photon absorption is a third-order nonlinear process and hence it should be very weak in comparison with one-photon absorption which is a linear process.

It should be marked that avalanche photodiode detected signals

from all area of the sample. However, it might be too weak to be detected by a spectrometer hence the nature of this signal cannot be determined. The possibility that it is noise should not be ignored. However, the material can be improved by slight increase of DAST in monomers. Nevertheless, if the concentration of DAST excides 1% of IDA+TMP mixture, it can cause a dramatic decrease of the viscosity due to the huge amount of methanol in solution and hence loss of thickness and quality of the film.

In conclusion, this method of simultaneous polymerization of monomers and synthesis of submicron DAST crystals can be improved by applying the interference pattern. This method supposes that polymerized monomers will start concentrating in bright light zones while DAST crystals will be pushed to the dark zones.

It was estimated that the best IDA : TMP ratio lies between 5:5 and 6:4. In this case, DAST concentration in IDA/TMP solution was 0.5%. The appropriate annealing temperature was 80°C and the annealing duration was around 1.5 hours. The examination of nonlinear properties showed clear SH signal from DAST crystals. Most of crystals were bigger than 1 μm. However, SHG was not observed from small DAST crystals. First reason might be not properly formed crystals and second reason might be very weak signal from smaller crystals compared with big DAST crystals.

3.3 Methods of fabrication of 3D nonlinear periodic structures

3.3.1 Holographic writing on nanocomposites

The first method is based on holographic writing in material described in subsection 3.2.1. A polymerization process lowers the chemical potential of monomers in the bright regions, leading to diffusion (short distance transportation) of monomers from the dark to the bright regions [70]. Hence, simultaneously synthesized DAST crystals transfer into dark regions. This method allows to write 1D, 2D and 3D structures depending on holographic setup. In this subsection, 1D periodic structure was written to prove the process of particles diffusion.

Solution of monomers IDA (408956 ALDRICH) and TMP (415871 ALDRICH) was mixed in proportion 1:1. DAST (CAS: 80969-52-4 Genolite biotek) was dissolved in methanol and then added to mixture of monomers. For all solutions, DAST amounted to 2% of IDA+TMP mixture. To start polymerization reaction, In2 (196118 Aldrich) was added and it equaled to 0.2% of monomers mixture. Spincoating rate was adjusted to get the samples with the thickness equal $\sim$3 μm.

The sample polymerization was provided by a simple holographic setup with two coherent laser beams. The setup consisted of the laser Cobolt Zouk^{TM} (continuous-wave mode with wavelength 355 nm, power $\leq$ 20 mW), lenses system forming collimated laser beam, prism

divided one laser beam into two coherent beams, and mirrors. The angle of two laser beams was changed by changing position of the mirrors. Hence the period of the 1D grating was also changed.

Figure 3.21 shows microphotographs of two samples. The first one was polymerized by an uniform collimated laser beam. The second one was polymerized by the holographic setup and shows the structure with a period of 5,5 μm. The exposition time was 10 min. After exposition, the diffraction of 1D grating can be observed by eye. Then, the sample was extra-exposed by an uniform collimated laser beam during 10 min, but the diffraction still exists. Both samples were analyzed in transmitting light by microscope Nikon Eclipse Ci-S and in reflecting light by microscope Leica DM2700 M (see Figure 3.21).

It is shown that there is a record of the volume hologram when two-beam interference is used. Microphotographs prove the movement of DAST nanoparticles in volume that provides creation of nonlinear gratings, which can be used for quasi-phase matching of nonlinear effects.

3.3.2 Photo-thermal destruction of DAST crystal by direct laser writing

The second method is focused on local photo-thermal destruction of nonlinear crystals by a direct laser writing. Multiphoton lithography is a well-known technique based on multiphoton absorption effects which

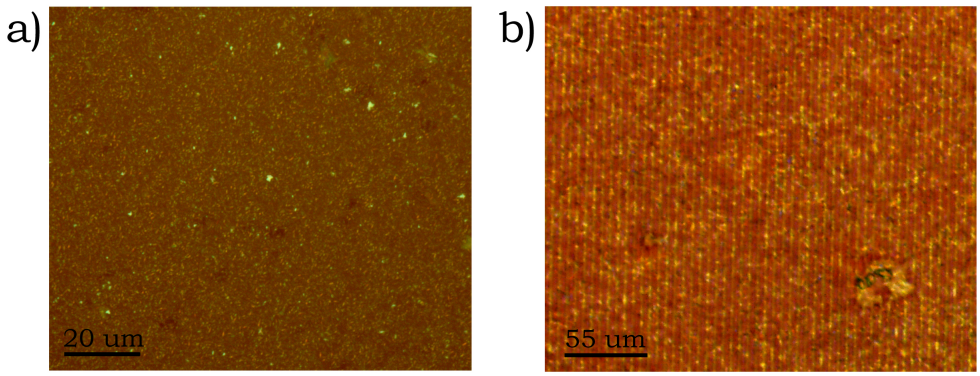

Figure 3.11: Microphotographs: a) sample, polymerized by an uniform collimated laser beam; b) 1D periodic structure with period 5,5 μm, generated by a holographic template.

allows to affect on material in focused spot and to write a structure in photoresist materials. This subsection proposes similar process to obtain a designed nonlinear structure.

DAST crystals have an absorption peak at the wavelength around 532 nm. High level of absorption can cause destabilization of crystalline form and subsequent transition into amorphous form. That leads to local loss of nonlinear properties of material. Subsection 3.2.1 proved that nonlinear optical properties are not affected by the size of crystals hence thick PMMA films with DAST crystals can be prepared. However preliminary 2D structure can approve this method and allow to analyze the result.

For this purpose a sample was prepared using a solution with a concentration 5% of DAST + PMMA in chloroform. DAST mass in solutions is equal to 2% of the PMMA mass. The film was spincoated by two-step centrifuging: first step is 100 rpm and second step 1500

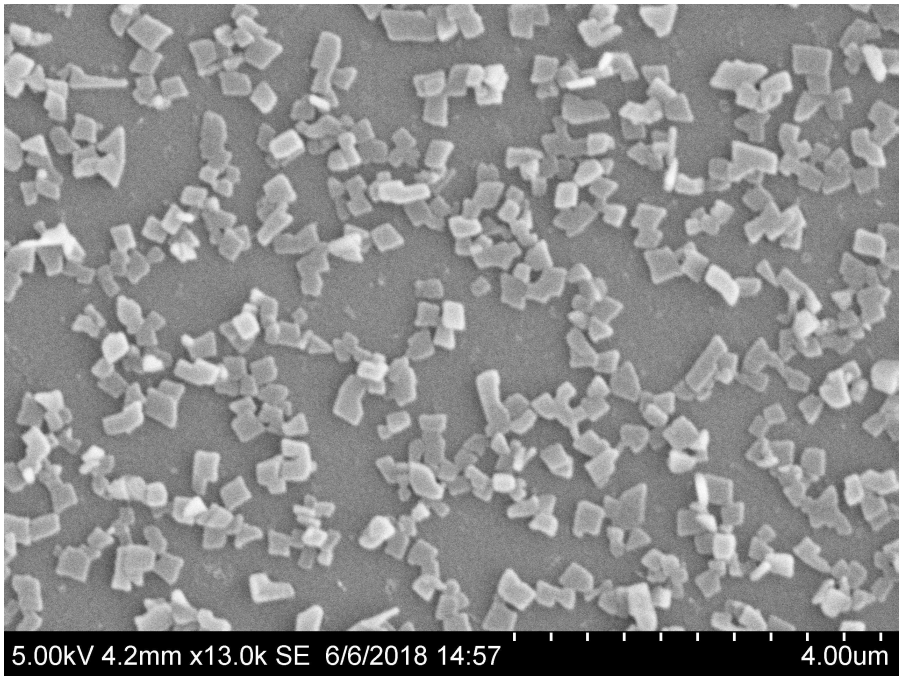

Figure 3.12: SEM-image of DAST crystals synthesized from solution with concentration 5% of PMMA+DAST in chloroform.

rpm for 10 s. Annealing was performed at 180°C for 30 min. Figure 3.12 presents SEM image of DAST crystals where average size of crystals is 300 nm. Thickness of the sample is 2 μm.

The LOPA DLW setup presented in subsection 3.2.2 (see Figure 3.9) was used to destruct crystals by photo-thermal effect caused by 532-nm laser. The power of the laser was changed for different purposes: first, for direct laser writing with high laser power and second for scanning the same area with very low power to detect by avalanche photodiode loss of fluorescence signal. A piezoelectric translator allows moving the sample very precise relative fixed and focused laser beam. By combining with an electronic shutter, it is possible to write dot by dot for any

image. The size of writing spot depends on parameters of the laser and also on parameters of the material itself. The experiment showed that the writing sport for a particular sample was about 1 μm. The written image was scanned without change of position of the sample to measure fluorescence. Then the image was examined by an optical microscope Nikon Eclipse Ci-S.

For direct laser writing, a lattice made of 5x5 lines with a period of 15 μm was proposed. The writing speed and the laser power beam directly influence on the quality of writing structures. During experiment, the power of the laser was changed, 1 mW, 5 mW and 10 mW. The speed of writing was varied from 5 to 35 μm/s.

The impact of laser radiation on a nanocomposite results in loss of DAST crystals fluorescence without any visible damages of the polymer film. It is caused by heating of DAST crystals due to high absorption of 532-nm laser. Fast heating and fast cooling of DAST molecular crystal force crystals to pass into an amorphous form. Luminescence of amorphous DAST has a quantum yield about 0.2%. It is much weaker in comparison with a crystal form, which shows the quantum yield of 14 - 20% [68]. For these reasons, the mechanism of the direct laser writing on a nanocomposite is based on photo-thermally destruction of DAST crystal with transformation to an amorphous form.

The experiment showed that with a power of 1 mW and a speed of writing 5 μm/s, the recording proceeds too slow. In this case, the thermal influence of the absorbed radiation destroyed surrounding crystals.

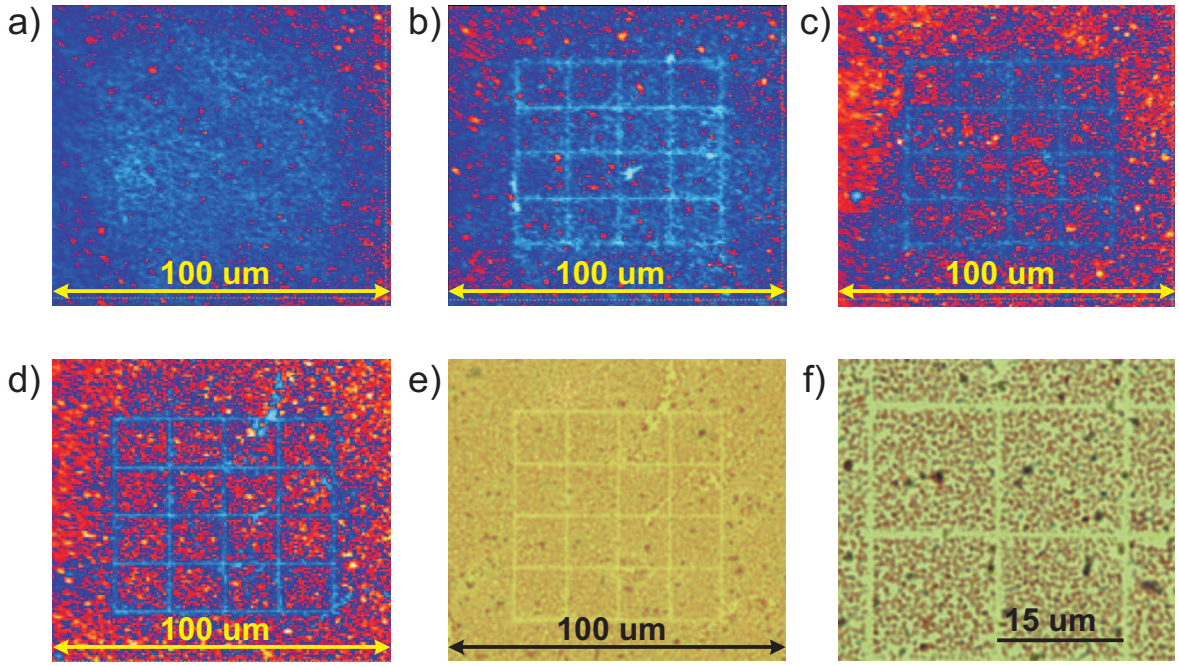

Figure 3.13: Color mapping of fluorescence signal after different combinations of writing parameters, which can be presented as couple "power – speed": a) 1 mW - 5 μm/s; b) 5 mW - 5 μm/s; c) 5 mW - 10 μm/s; d) 10 mW - 35 μm/s. e) – f) Photos of the sample recorded with a power of 10 mW and a speed of 35 μm/s and taken by an optical microscope.

Figure 3.22a clearly demonstrates that the speed and power of writing should be increased.

Increase of power up to 5 mW allowed creating more accurately set image, however the thermal influence on surrounding crystals is still seen in the Figure 3.22b, because of the slow speed of laser writing. Double increase of writing speed up to 10 μm/s improved quality of recorded image, as shown in Figure 3.22c.

According these results, the direct laser writing requires high power and high speed rate.Figure 3.22d presents mapping of fluorescence signal received after direct laser writing at the power 10 mW and at

the speed 35 μm/s. Width of the written down line does not exceed 1 μm. That is connected with a high absorption of material at wavelength 532 nm, with a high writing speed and with the size of DAST crystals (300 μm), which is smaller than the writing spot. Lines of destroyed crystals can be clearly observed at the optical microscope (Figure 3.22e-f). Studying of the sample surface on profilometer (Dektak 150) revealed that there are no relief changes of the sample and PMMA was not affected by thermal influence.

As a result, a 2D structure in PMMA film with submicron nonlinear crystals of DAST were recorded by direct laser writing. Therefore, it is possible to write down QPM structure with the precise period. Width of the line was about 1 μm and direct laser writing did not produce visible destructions of a PMMA layer. A thermal influence on surrounding crystals at the low speed writing and an absence of relief changes at PMMA layer allow to suggest polymorphic transformation of nanocrystals.

The wavelength of 532-nm laser lays in the middle of the absorption peak of nanocomposites. Hence this setup allows writing down only 2D images. Writing 3D images requires two-photon absorption. For this purpose the powerful infrared laser should be implemented into setup. Modified setup will provide the prospect to fabricate 3D QPM structure.

3.3.3 Synthesis of DAST crystals in voids of SU-8 template

The main idea of this method is fabrication of SU-8 template using an interference technique, because it results into large sample with good quality and uniformity. SU-8 is a well-known photoresist which allows to fabricate any 2D and 3D structures[64]. Then PMMA/DAST solution from section 3.2.1 can be dropped on the template, spincoated and annealed to provide DAST crystallization. That will lead to a spatial deposition of nonlinear DAST crystals which will be concentrated in small voids of the linear material (SU-8 template). This method was proved by fabrication of a 2D nonlinear periodic structure.

The process of template fabrication starts with surface treatment to improve the adhesion of photoresists to substrates and to get a good sample. SU-8 2002 (Micro. Chem. Corp.) was spin-coated into glass substrate with a thickness of 2 μm. To remove the solvent, the film was soft baked for 1 min at 65°C and then for 2 min at 95°C. A continuous UV laser (Cobalt) with $\lambda = 355$ nm was used to expose the SU-8 sample by two-beam interference technique, because the absorption of SU-8 photoresist is in the range of 300-400 nm. Post baking proceeded for 5 min on a hot plate at 95°C to improve cross-linking of the polymerized resin. Finally, the sample was developed for 4 min in SU-8 developer and dissolved photoresist was removed by isopropanol and DI water. Figure 3.14 shows the uniformity of fabricated samples.

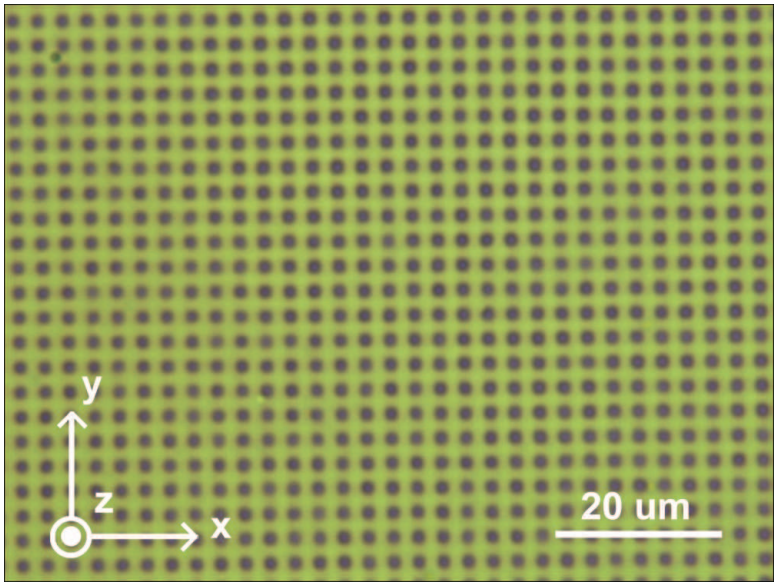

Figure 3.14: SU-8 template with a period of 3 μm.

Its period equals 3 μm.

It should be noted that unfortunately it is not possible to mix SU-8 and DAST powder directly because SU-8 or much more likely its solvents dissolve DAST. However, even solid template of SU-8 prevents synthesis of DAST crystals in voids due to the remained solvents. That drawback can be overcome by SU-8 hard baking. Sample was hard baked for 40 min at 180°C.

For this experiment, it is proposed to use the same DAST/PMMA solution with a concentration of 5% of DAST + PMMA in chloroform. DAST mass in solutions is equal to 2% of the PMMA mass. DAST/PMMA solution was dropped on the SU-8 template and spin-coated at low speed rate to remove extra solution from the top. Then the sample was annealed at 180°C for 30 min.

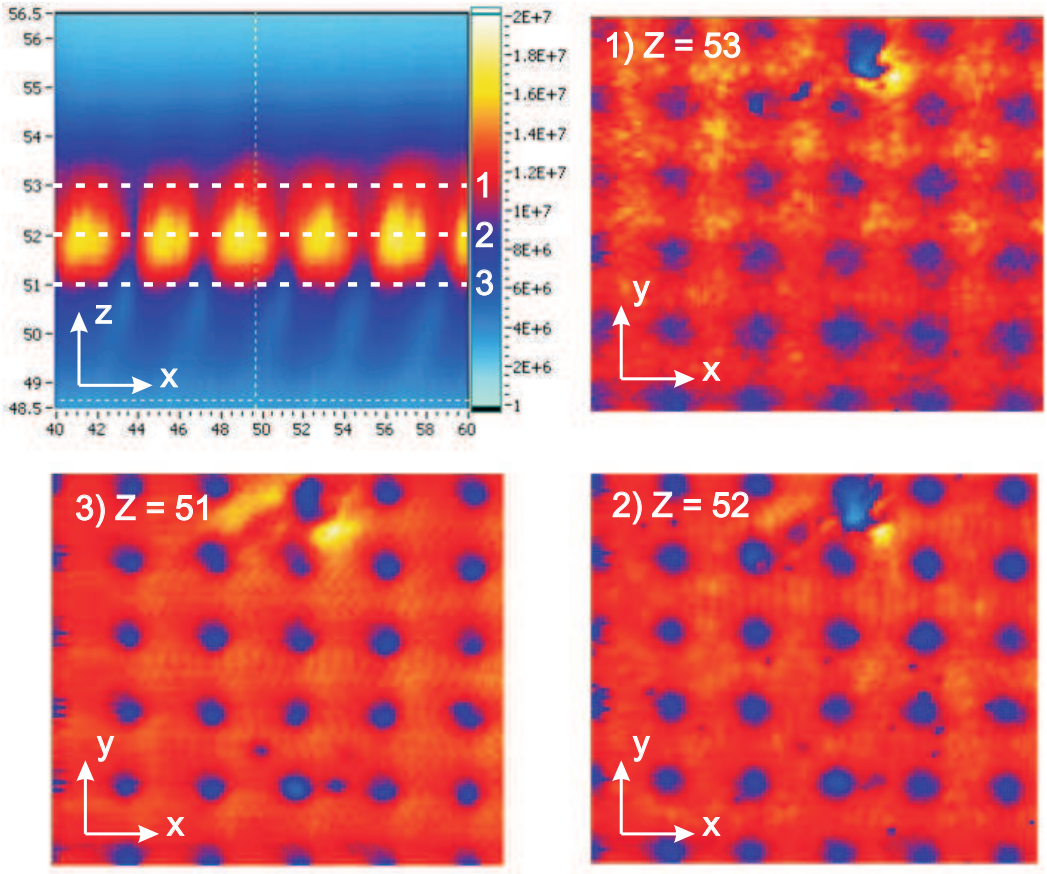

Figure 3.15: Fluorescence mapping of fabricated sample by scanning one ZX-plane and three XY-planes at different positions of Z.

Characterization of the nonlinear sample can be done by LOPA DLW setup described in subsection 3.2.2 (see Figure 3.9). A 532-nm laser was used as a scanner to detect powerful signal of DAST crystals in comparison with SU-8 signal. The fluorescence mapping of ZX-plane scan can be observed in Figure 3.15. It assures that thickness of the sample is 2 μm. Fluorescence mapping of XY-planes shows periodical pattern comparable with the sample from Figure 3.14. According to Figure 3.15 the template is well fulfilled by DAST crystals.

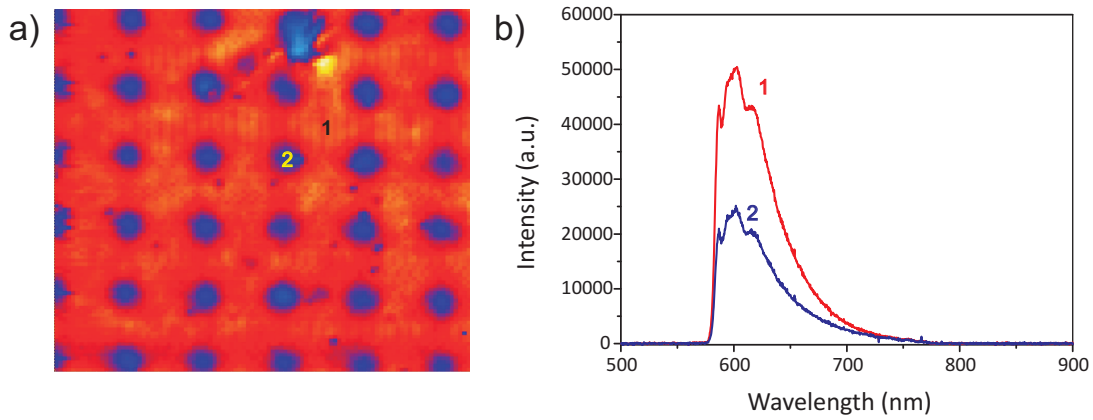

Figure 3.16: a) Fluorescence mapping of SU-8 template by scanning XY-planes at fixed Z-positions and b) fluorescence spectra of two points in the sample, where line 1 corresponds to DAST fulfilled area and line 2 corresponds to SU-8 area.

Figure 3.16b shows fluorescence spectra of two points in the sample, where line 1 corresponds to DAST fulfilled area and line 2 corresponds to SU-8 area. First of all, a twice weaker signal is observed from the SU-8 area. Second, both curves have the same shape. That means that the source of this spectrum is the same hence this second spectrum is light bias from DAST area. Excitation spectrum of 532-nm laser was blocked by a 580-nm long-pass filter that is the reason of sharp cut in green area.

In order to examine the SHG signal, a 1064-nm laser was used. Figure 3.17 shows SH mapping of the sample by scanning one ZX-plane and three XY-planes at different positions of Z. Obviously it has some problems with alignment between two lasers, because Z position of fluorescence and SHG differs. However periodic pattern at two XY-planes can be clearly seen.

The presence of SHG signals was examined by a spectrometer. Fig-

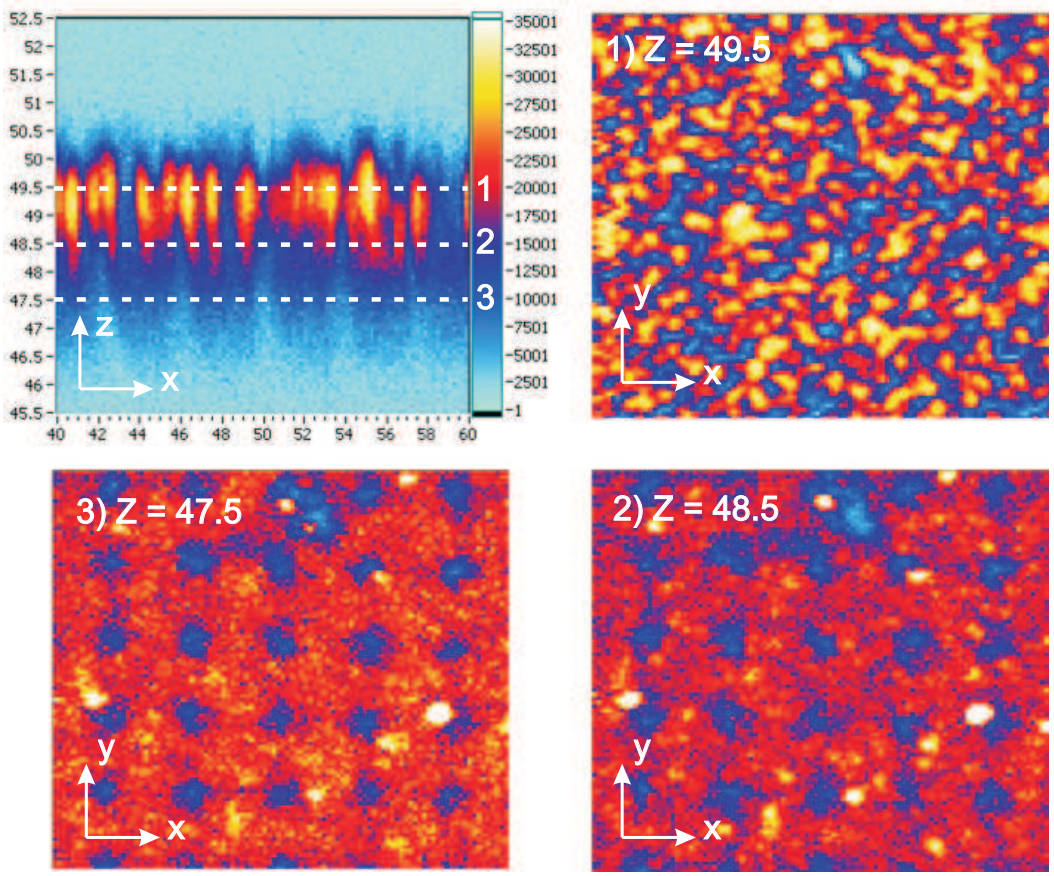

Figure 3.17: SH mapping by scanning one ZX-plane and three XY-planes at different positions of Z.

ure 3.23 displays SH mapping of the sample by scanning XY-planes at fixed Z-positions and SH spectra of two points in the sample, where line 1 corresponds to DAST fulfilled area and line 2 corresponds to SU-8 area. A narrow pick at 532 is well-observed. Hence, DAST crystals in SU-8 template have nonlinear properties. Second spectrum seems to be again alight bias from DAST area.

In conclusion, this method is very perspective for spatial deposition of nonlinear material. It can be used for fabrication of 3D QPM

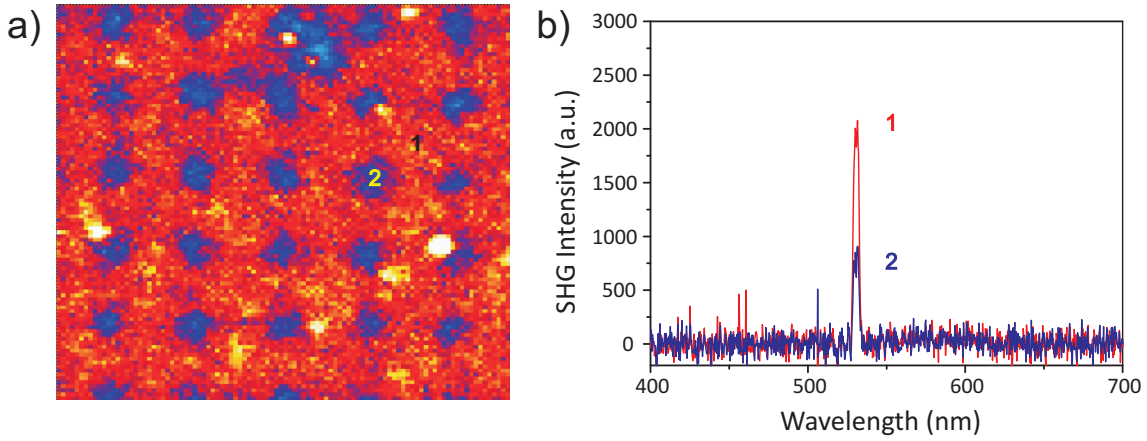

Figure 3.18: a) SH mapping by scanning XY-planes at fixed Z-positions and b) SH spectra of two points in the sample, where line 1 corresponds to DAST fulfilled area and line 2 corresponds to SU-8 area.

structures. There might be a problem with leaking of solution inside 3D SU-8 template. However, this method is also very prospective.

3.4 Conclusion

This chapter presented the investigation of two nanocomposite materials with embedded crystals of DAST which provide nonlinear properties. First material consists of PMMA with synthesized DAST crystals of controllable size, which depends on the film thickness. First-ever, it was investigated the dependence of second-order nonlinear optical coefficient of DAST crystals on its size in micron and submicron scale. Investigation showed that nonlinear coefficient does not have dimensional dependence, even if crystals decrease till size of tens of nanometers.

Second nanocomposite material consists of polymerizable mixture of monomers and dissolved DAST. It is useful for holographic writing in material with induced transfer of crystallized DAST into dark zones. Therefore, a 1D nonlinear periodic structure was fabricated by holographic writing on photopolymerized nanocomposite with nonlinear submicron DAST crystals. This method and material allow to write 1D, 2D and 3D nonlinear structures depending on setup.

Another method of 2D nonlinear lattice fabrication is based on direct laser writing in the film of PMMA with embedded submicron DAST crystals. A 2D nonlinear lattice was fabricated using this method. It induces photothermal destruction of DAST crystals with transition to amorphous form and without any surface destruction.

The third method of 2D nonlinear lattice fabrication is based on filling voids of SU-8 photoresist template with PMMA/DAST composite and a 2D nonlinear lattice was fabricated using this method. Annealing at high temperature causes synthesis of nonlinear DAST crystals inside voids. SU-8 photoresist is a well-known material for fabrication of 3D structures; hence described method is prospective for fabrication of 3D QP structures.

Conclusions and prospects

This work demonstrated investigation of 3D QPM structures through different aspects. Firstly it presented a full analysis of SHG efficiency in 3D QPM periodical lattice mathematically modeled as convolution product of a crystal lattice and a motif. It was demonstrated that efficiency of SHG strongly depends on parameters of lattice and motif. As a result, it was shown that the most perspective combination was a cubic lattice with a spherical motive. This structure can be fabricated by interference techniques using specially synthesized material.

Following this statement, two prospective nanocomposites were synthesized and examined. The first one consists of PMMA film with embedded nonlinear submicron DAST crystals. The examination of the dependence of second-order nonlinear optical coefficient of DAST crystals on its size in micron and submicron scale showed neglectable decreases, which means absence of dimensional dependence of this co-

efficient.

This material was used for fabrication of 2D nonlinear structures by two different methods. The first method was based on direct laser writing which caused photo-thermal destruction of DAST crystals and its transition to an amorphous form and hence local loss of nonlinear properties. The best structure quality was achieved by the following parameters: laser at 532 nm, power was 35 mW, speed of writing was 10 μm/s. The width of smallest written line was 1 μm.

The second method was based on fabrication of SU-8 templates and filling voids with nonlinear PMMA/DAST nanocomposite. Fabricated SU-8 templates had 2 μm thickness and 3 μm periodicity. To achieve the formation of nonlinear crystals of DAST, empty SU-8 templates required hard baking at a temperature of $180 - 200$°C within 30-60 minutes depending on thickness and complexity of a sample. Sample was annealed one more time after filing voids at $180 - 200$°C for DAST crystallization.

The second synthesized material provided simultaneous polymerization of monomers and synthesis of submicron DAST crystals. The interference technique can cause mass-transfer of DAST crystals into dark zones and polymerized monomers into light zones; hence this method can fabricate 1D, 2D and 3D nonlinear periodic structures depending on fabrication setup.

Following this work, several prospects are proposed:

- Increasing thickness of PMMA/DAST films and building a setup for direct-laser writing by two-photon absorption to fabricate 3D QPM structures.

- Fabricating 3D SU-8 templates and examining limitations of structures period connected with possibility to fill voids by PMMA/DAST composite.

- Fabricating 2D and 3D periodical nonlinear structures by interference technique or by lithographic mask in material based on polymerizable nanocoposite with monomers and DAST crystals.

Bibliography

[1] Franken, P. A., Hill, A. E., Peters, C. W., and Weinreich, G., "Generation of optical harmonics," *Phys. Rev. Lett.* **7**, 118 (1961).

[2] Maiman, T. H., "Stimulated optical radiation in ruby," *Nature* **187**, 493 (1960).

[3] Saleh, B. E. A. and Teich, M. C., [*Fundamentals of photonics*], New York: Wiley (1991).

[4] Bloembergen, N., [*Nonlinear Optics*], World Scientific Pub Co Inc (1996).

[5] Shen, Y. R., [*The principles of nonlinear optics*], Wiley-Interscience (2002).

[6] Broderick, N. G. R., Ross, G. W., Offerhausa, H. L., Richardson, D. J., and Hanna, D. C., "Hexagonally poled lithium niobate: a two-dimensional nonlinear photonic crystal," *Phys. Rev. Lett.* **84**, 4345 (2000).

[7] Chowdhury, A., Staus, C., Boland, B. F., Kuech, T. F., and McCaughan, L., "Experimental demonstration of 1535–1555-nm simultaneous optical wavelength interchange with a nonlinear photonic crystal," *Opt. Lett.* **26**, 1353 (2001).

[8] Broderick, N. G. R., Bratfalean, R. T., Monro, T. M., Richardson, D. J., and de Sterke, C. M., "Temperature and wavelength tuning of second-, third-, and fourth-harmonic generation in a two-dimensional hexagonally poled nonlinear crystal," *J. Opt. Soc. Am. B* **19**, 2263 (2002).

[9] Saltiel, S. M. and Kivshar, Y. S., "Phase matching in nonlinear x(2) photonic crystals," *Opt. Lett.* **25**, 1204 (2000).

[10] Saltiel, S. M. and Kivshar, Y. S., "All-optical deflection and splitting by second-order cascading," *Opt. Lett.* **27**, 921 (2002).

[11] Vodopyanov, K. L., Levi, O., Kuo, P. S., Pinguet, T. J., Harris, J. S., Fejer, M. M., Gerard, B., Becouarn, L., and Lallier, E., "Optical parametric oscillation in quasi-phase-matched gaas," *Opt. Lett.* **29**, 1912 (2004).

[12] Trajtenebrg-Mills, S. and Arie, A., "Shaping light beams in nonlinear processes using structured light and patterned crystals," *Opt. Mat. Express* **7**, 2928 (2017).

[13] Hu, X. P., Xu, P., and Zhu, S. N., "Engineered quasi-phase-matching for laser techniques," *Photonics Research* **1**, 171 (2013).

[14] Zhang, X., Lytle, A. L., Popmintchev, T., Zhou, X., Murnane, M. M., Kapteyn, H. C., and Cohen, O., "Quasi phase matching and quantum path control of high harmonic generation using counterpropagating light," *Nature Physics* **4**, 270 (2007).

[15] Caspani, L., Xiong, C., Eggleton, B., Bajoni, D., Liscidini, M., Galli, M., Morandotti, R., and Moss, D., "Integrated sources of photon quantum states based on nonlinear optics," *Light: Science & Applications* **6**, e17100 (2017).

[16] Tomita, I., Suzuki, H., Ito, H., Takenouchi, H., Ajito, K., Rungsawang, R., and Ueno, Y., "Terahertz-wave generation from quasi-phase-matched gap for 1.55 μm pumping," *Appl. Phys. Lett.* **88**, 071118 (2006).

[17] Avetisyan, Y. and Tonouchi, M., "Terahertz generation in quasi-phase-matching structure formed by a phase mask," *Opt. Lett.* **37**, 4155 (2012).

[18] Giordmaine, J. A., "Mixing of light beams in crystals," *Phys. Rev. Lett.* **8**, 19 (1962).

[19] Maker, P. D., Terhune, R. W., Nisenoff, M., and Savage, C. M., "Effects of dispersion and focusing on the production of optical harmonics," *Phys. Rev. Lett.* **8**, 21 (1962).

[20] Danielius, R., Piskarskas, A., Trapani, P. D., Andreoni, A., Solcia, C., and Foggi, P., "Matching of group velocities by spatial walk-off in collinear three-wave interaction with tilted pulses," *Opt. Lett.* **21**, 973 (1996).

[21] Armstrong, D. J., Alford, W. J., Raymond, T. D., Smith, A. V., and Bowers, M. S., "Parametric amplification and oscillation with walkoff-compensating crystals," *J. Opt. Soc. Am. B* **14**, 460 (1997).

[22] Smith, A. V., Armstrong, D. J., and Alford, W. J., "Increased acceptance bandwidths in optical frequency conversion by use of multiple walk-off-compensating nonlinear crystals," *J. Opt. Soc. Am. B* **15**, 122 (1998).

[23] Armstrong, J. A., Bloembergen, N., Ducuing, J., and Pershan, P. S., "Interactions between light waves in a nonlinear dielectric," *Phys. Rev.* **127**, 1918 (1962).

[24] Fejer, M. M., Magel, G. A., Jundt, D. H., and Byer, R. L., "Quasi-phase-matched second harmonic generation: tuning and tolerances," *IEEE J. Quant. Electron.* **28**, 2631 (1992).

[25] Hum, D. S. and Fejer, M. M., "Quasi-phasematching," *C. R. Physique* **8**, 180 (2007).

[26] Arie, A. and Voloch, N., "Periodic, quasi-periodic, and random quadratic nonlinear photonic crystals," *Laser & Photon. Rev.* **4**, 355 (2010).

[27] Berger, V., "Nonlinear photonic crystals," *Phys. Rev. Lett.* **81**, 4136 (1998).

[28] Xu, P., Li, K., Zhao, G., Zhu, S., Du, Y., Ji, S., Zhu, Y., Ming, N., Luo, L., Li, K., and Cheah, K., "Quasi-phase-matched generation of tunable blue light in a quasi-periodic structure," *Opt. Lett.* **29**, 95 (2004).

[29] Porat, G., Gayer, O., and Arie, A., "Simultaneous parametric oscillation and signal-to-idler conversion for efficient downconversion," *Opt. Lett.* **35**, 1401 (2010).

[30] Ren, M. L., Ma, D. L., and Li, Z. Y., "Experimental demonstration of super quasi-phase matching in nonlinear photonic crystal," *Opt. Lett.* **36**, 3696 (2011).

[31] Sheng, Y., Ma, D., Ren, M., Chai, W., Li, Z., Koynov, K., and Krolikowski, W., "Broadband second harmonic generation in one-dimensional randomized nonlinear photonic crystal," *Appl. Phys. Lett.* **99**, 031108 (2011).

[32] Yamada, M., Nada, N., Saitoh, M., and Watanabe, K., "First-order quasi-phase matched $LiNbO_3$ waveguide periodically poled by applying an external field for efficient blue second-harmonic generation," *Appl. Phys. Lett.* **62**, 435 (1993).

[33] Eyres, L. A., Tourreau, P. J., Pinguet, T. J., Ebert, C. B., Harris, J. S., Fejer, M. M., Becouarn, L., Gerard, B., and Lallier, E., "All-epitaxial fabrication of thick, orientation-patterned GaAs films for nonlinear optical frequency conversion," *Appl. Phys. Lett.* **79**, 904 (2001).

[34] Rikken, G. L. J. A., Seppen, C. J. E., Nijhuis, S., and Meijer, E. W., "Poled polymers for frequency doubling of diode lasers," *Appl. Phys. Lett.* **58**, 435 (1991).

[35] Yilmaz, S., Bauer, S., and Gerhard-Multhaupt, R., "Photothermal poling of nonlinear optical polymer films," *Appl. Phys. Lett.* **64**, 2770 (1994).

[36] Taggi, V., Michelotti, F., Bertolotti, M., Petrocco, G., Foglietti, V., Donval, A., Toussaere, E., and Zyss, J., "Domain inversion by pulse poling in polymer films," *Appl. Phys. Lett.* **72**, 2794 (1998).

[37] Apostoluk, A., Chapron, D., Gadret, G., Sahraoui, B., Nunzi, J., Fiorini-Debuisschert, C., and Raimond, P., "Quasi-phase-matched gratings printed by all-optical poling in polymer films," *Opt. Lett.* **27**, 2028 (2002).

[38] Martin, G., Ducci, S., Hierle, R., Josse, D., and Zyss, J., "Quasiphase matched second-harmonic generation from periodic optical randomization of poled polymer channel waveguides," *Appl. Phys. Lett.* **83**, 1086 (2003).

[39] Sugihara, O., Nakanishi, M., Che, Y., Egami, C., Kawata, Y., and Okamoto, N., "Single-pulse ultraviolet laser recording of periodically poled structures in polymer thin films," *Appl. Opt.* **39**, 5632 (2000).

[40] Ni, X., Nakanishi, M., Sugihara, O., and Okamoto, N., "Fabrication of x(2) grating in poled polymer waveguide based on direct laser beam writing," *Opt. Rev.* **5**, 9 (1998).

[41] Lin, J. H., Lai, N. D., Chiu, C. H., Lin, C. Y., Rieger, G. W., Young, J. F., Chien, F. S. S., and Hsu, C. C., "Fabrication of spatial modulated second order nonlinear structures and quasi-phase matched second harmonic generation in a poled azo-copolymer planar waveguide," *Opt. Exp.* **16**, 7832 (2008).

[42] Chen, J. and Chen, X., "Phase matching in three-dimensional nonlinear photonic crystals," *Phys. Rev. A* **80**, 013801 (2009).

[43] Chen, J. and Chen, X., "Generation of conical and spherical second harmonics in three-dimensional nonlinear photonic crystals with radial symmetry," *J. Opt. Soc. Am. B* **28**, 241 (2011).

[44] Pogosian, T. and Lai, N. D., "Theoretical investigation of three-dimensional quasi-phase-matching photonic structures," *Phys. Rev. A* **94**, 063821 (2016).

[45] Russel, S. M., Powers, P. E., Missey, M. J., and Scheple, K. L., "Broadband mid-infrared generation with two-dimensional quasi-phase-matched structures," *IEEE J. Quant. Electron.* **37**, 877 (2001).

[46] Xavie, J., Rose, P., Terhalle, B., Joseph, J., and Denz, C., "Three-dimensional optically induced reconfigurable photorefractive nonlinear photonic lattices," *Opt. Lett.* **34**, 2625 (2009).

[47] Farsari, M., Ovsianikov, A., Vamvakaki, M., Sakellari, I., Gray, D., Chichkov, B. N., and Fotakis, C., "Fabrication of three-dimensional photonic crystal structures containing an active nonlinear optical chromophore," *Appl. Phys. A* **93**, 11 (2008).

[48] Do, D. B., Lin, J. H., Lai, N. D., Kan, H. C., and Hsu, C. C., "Fabrication of three-dimensional polymer quadratic nonlinear grating structures by layer-by-layer direct laser writing technique," *Appl. Opt.* **50**, 4664 (2011).

[49] Xu, T., Lu, D., Yu, H., Zhang, H., Zhang, Y., and Wang, J., "A naturally grown three-dimensional nonlinear photonic crystal," *Appl. Phys. Lett.* **108**, 051907 (2016).

[50] Xu, T., Switkowski, K., Chen, X., Liu, S., Koynov, K., Yu, H., Zhang, H., Wang, J., Sheng, Y., and Krolikowski, W., "Three-dimensional nonlinear photonic crystal in ferroelectric barium calcium titanate," *Nat. Photonics* **12**, 591 (2018).

[51] Wei, D., Wang, C., Wang, H., Hu, X., Wei, D., Fang, X., Zhang, Y., Wu, D., Hu, Y., Li, J., Zhu, S., and Xiao, M., "Experimental demonstration of a three-dimensional lithium niobate nonlinear photonic crystal," *Nature Photonics* **12**, 596 (2018).

[52] Ruiz, B., Jazbinsek, M., and Gunter, P., "Crystal growth of dast," *Crystal Growth & Design* **8**, 4173 (2008).

[53] Chen-Yang, Y., Sheu, T., Lin, S., and Tu, Y., "Morphology and lightguide property investigation of a high quality dast single crystal," *Current Applied Physics* **2**, 349 (2002).

[54] Coe, B. J., Hall, J. J., Harris, J. A., Brunschwig, B. S., Coles, S. J., and Hursthouse, M. B., "Trans-4-[(4-Dimethylaminophenyl)ethenyl]-N-methylquinolinium p-toluenesulfonate monohydrate," *Acta Cryst.* **E61**, o464 (2005).

[55] Zheng, M. L., Chen, W. Q., Fujita, K., Duan, X. M., and Kawata, S., "Dendrimer adjusted nanocrystals of DAST: organic crystal with enhanced nonlinear optical properties," *Nanoscale* **2**, 913–916 (2010).

[56] Zheng, M. L., Fujita, K., Chen, W. Q., Duan, X. M., and Kawata, S., "Two-photon excited fluorescence and second-harmonic generation of the dast organic nanocrystals," *J. Phys. Chem. C* **115**, 8988 (2011).

[57] Oikawa, H., Fujita, S., Kasai, H., Okada, S., Tripathy, S. K., and Nakanishi, H., "Electric field-induced orientation of organic microcrystals with large dipole moment in dispersion liquid," *Colloids and Surfaces A Physicochem. Eng. Aspects* **169**, 251 (2000).

[58] Kaneko, Y., Shimada, S., Fukuda, T., Kimura, T., Yokoi, H., Matsuda, H., Onodera, T., Kasai, H., Okada, S., Oikawa, H., and Nakan, H., "A novel method for fixing the anisotropic orientation of dispersed organic nanocrystals in a magnetic field," *Adv. Mater.* **17(2)**, 160 (2005).

[59] Macchi, R., Cariati, E., Marinotto, D., Roberto, D., Tordin, E., Ugo, R., Bozio, R., Cozzuol, M., Pedron, D., and Mattei, G., "Stable SHG from in situ grown oriented nanocrystals of [(E)-N,N-dimethylamino-N'-methylstilbazolium][p-toluenesulfonate] in a PMMA film," *J. Mater. Chem.* **20**, 1885 (2010).

[60] Burunkova, J. A., Denisyuk, I. Y., and Fokina, M. I., "Polymer composite based on DAST submicron crystals: technology and properties," *Mol. Cryst. Liq. Crys.* **589**, 178 (2014).

[61] Kittel, C., [*Introduction to Solid State Physics*], New York: Wiley (1995).

[62] Arie, A., Habshoosh, N., and Bahabad, A., "Quasi phase matching in two-dimensional nonlinear photonic crystals," *Opt. Quant. Electron.* **39**, 361 (2007).

[63] Ho, K. M., Chan, C. T., and Soukoulis, C., "Existence of a photonic gap in periodic dielectric structures," *Phys. Rev. Lett.* **65**, 3152 (1990).

[64] Lai, N. D., Liang, W. P., Lin, J. H., Hsu, C. C., and Lin, C. H., "Fabrication of two- and three-dimensional periodic structures by multi-exposure of two-beam interference technique," *Opt. Express* **13**, 9605 (2005).

[65] Lai, N. D., Do, D. B., Lin, J. H., and Hsu, C. C., "Fabrication of desired three-dimensional structures by holographic assembly technique," *Appl. Phys.* **100**, 171 (2010).

[66] Li, Q., Do, M. T., Ledoux-Rak, I., and Lai, N. D., "Concept for three-dimensional optical addressing by ultralow one-photon absorption method," *Opt. Lett.* **38**, 4640–4643 (2013).

[67] Thomas, T., Ramaclus, J. V., Mena, F. P., Mosquera, E., Sagayaraja, P., and Michaelb, E. A., "Influence of oleic acid on the nucleation and growth of 4-N,N-dimethylamino-

4-N-methyl-stilbazoliumtosylate (DAST) crystals," *CrystEngComm* **17**, 1989–1996 (2015).

[68] Bhowmik, A. K., Xu, J., and Thakur, M., "Polarized optical absorption and photoluminescence measurements in single-crystal thin films of 4'-dimethylamino-N-methyl-4-stilbazolium tosylate," *Appl. Phys. Lett.* **75**, 3291 (1999).

[69] Kasai, H., Kaneko, Y., Onodera, T., Nakanishi, H., Oikawa, H., Okada, S., Shimada, S., Kimura, T., and Matsuda, H., "External field-induced orientation of dast naocrystals in the dispersion state and the fixation," *Proc. SPIE* **6891**, 689114 (2008).

[70] Tomita, Y. and Suzuki, N., "Holographic manipulation of nanoparticle distribution morphology in nanoparticle-dispersed photopolymers," *Opt. Lett.* **8**, 839 (2006).

Résumé an Français

Titre : Structures quasi-accord de phase 3D: étude théorique, élaboration de matériaux non-linéaires, et réalisation des structures en matériau polymère

Mots clés : Quasi-accord de phase ; polymère ; interference ; generation de seconde harmonique ; DAST nanocristal.

Quasi-accord de phase (QPM) 3D est très important pour l'optique non linéaire, mais il n'est pas encore étudié théoriquement et expérimentalement. Le manque d'intérêt pour l'étude des structures QPM 3D a été causé par l'extrême complexité de la fabrication. Par conséquent, les études théoriques de QPM 3D en optique non linéaire n'ont pas non plus été récompensées avec des attentions suffisantes. Le but de ce travail est d'étudier théoriquement et expérimentalement les structures QPM 3D dans des matériaux non linéaires. La thèse est divisée en trois tâches principales: i) analyse théorique de l'efficacité de la génération de seconde harmonique (SHG) dans un réseau QPM 3D; ii) synthèse et analyse de matériaux à base de polymères avec des particules submicroniques non linéaires incorporées pour fabriquer un réseau non linéaire; iii) développement de méthodes pour créer des réseaux QPM 2D et 3D non linéaires.

A – Analyse théorique de l'efficacité SHG dans un réseau QPM 3D : Dans cette partie, nous avons présenté la fonction de non-linéarité comme un produit de la susceptibilité non linéaire $\chi^{(2)}$

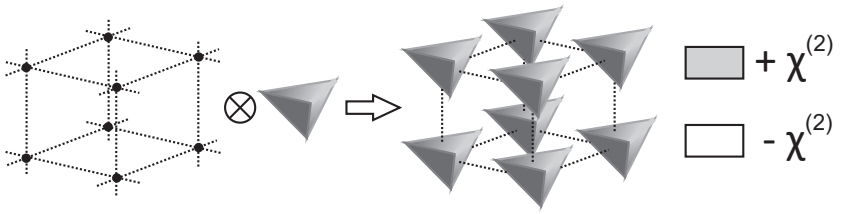

Figure 3.19: Convolution d'un simple treillis cubique avec un motif triangulaire pour obtenir une structure QPM périodique 3D.

tenseur et une fonction normalisée et sans unité $g(\mathbf{r})$, représentant la dépendance spatiale de $\chi^{(2)}$. Cette fonction a été décrite comme un produit de convolution d'un réseau périodique et d'un motif (Figure 1). Par conséquent, $g(\mathbf{r})$ a été représenté comme une série de Fourier.

Cela simplifie grandement l'analyse de la structure 3D avec le QPM car le coefficient de Fourier devient le paramètre le plus important pour l'efficacité de conversion du SHG. Le coefficient de Fourier dépend des paramètres du réseau et des motifs, par conséquent, nous nous intéressons à la combinaison la plus préférable de réseau et de motifs pour obtenir le rendement de conversion le plus élevé.

Premier temps, nous avons décrit des réseaux périodiques primitifs et réciproques qui sont basés sur des réseaux Bravais. Un tableau de ce travail fournit tous les paramètres de ces réseaux en fonction des coordonnées de référence choisies. Toutes les données ont été utilisées dans d'autres calculs. Deuxièmement, nous avons présenté le calcul de la Transformée de Fourier de motifs orthorhombiques, sphériques et cylindriques. Un autre tableau de ce travail montre les coefficients de Fourier pour les motifs orthorhombiques et sphériques, en fonction

du type de réseau. Nous avons démontré la dégénérescence des structures 3D dans des cas particuliers de structures 1D et 2D. Il a été démontré que, dans ces cas, les coefficients d'efficacité concordaient avec les données publiées précédemment. Semblable aux structures QPM 1D et 2D, les structures 3D ont également montré les coefficients les plus élevés pour le premier ordre QPM. Les coefficients de Fourier des structures QPM 3D étaient inférieurs aux coefficients des structures 2D.

Le prochain objectif de cette partie était d'optimiser et d'analyser les structures QPM 3D. Nous avons étudié des réseaux plus compliqués tels que le réseau cubique centré (BBC), le réseau cubique à faces centrées (FCC) ou le réseau de type "diamante"(DC). Nous avons remarqué que si une structure QPM fournit une plus grande quantité de vecteurs QPM, cela conduit à une efficacité plus faible de SHG. Nous prêtons également attention aux coefficients de Fourier pour les structures symétriques, telles que le réseau cubique avec des motifs cubiques ou sphériques, qui étaient plutôt élevés. Enfin, nous avons décrit une structure QPM compliquée avec des connexions entre des motifs qui représentent approximativement le motif réel à fabriquer. Le coefficient de Fourier calculé a montré que des connexions supplémentaires entre des motifs sphériques n'affectent pas l'efficacité de la structure QPM.

Les publications concernant ces travaux:

- Pogosian T., Lai N. // Theoretical investigation of three-dimensional quasi-phase-matching photonic structures // Physical Review A - 2016, Vol. 94, No. 6, pp. 063821.

B – Synthèse et analyse de matériaux pour la fabrication de réseaux non linéaires : Cette partie est consacrée à la synthèse et à l'analyse de matériaux nanocomposites à base de polymères et de monomères avec un cristal DAST (4-[4-(Dimethylamino)styryl]-1-methylpyridinium p-toluenesulfonate) submicronique non linéaire incorporé.

Le premier matériau nécessitait une solution de DAST liquid (méthanol comme solvant) et de polyméthacrylate de methyl (PMMA) liquid (chloroforme comme solvant). Pendant la préparation de l'échantillon, cette solution a été spin enduit sur le wafer de verre. Des cristaux ont été formés à partir de petites bulles de méthanol avec du DAST, qui cristallise lors de l'évaporation du solvant. Nous avons modifié la concentration des solvants et des produits chimiques, ainsi que les paramètres du revêtement et du recuit de spin pour révéler les dépendances de la croissance des cristaux. La Figure 2 montre des MEB-images d'échantillons avec différentes concentrations de solvant de départ (viscosité de la solution). En enlevant la couche de PMMA et en enduisant les cristaux restants à la surface avec un film d'Or, il a été possible d'examiner la morphologie des cristaux de DAST et d'étudier la dépendance des paramètres optiques linéaires et non linéaires en fonc-

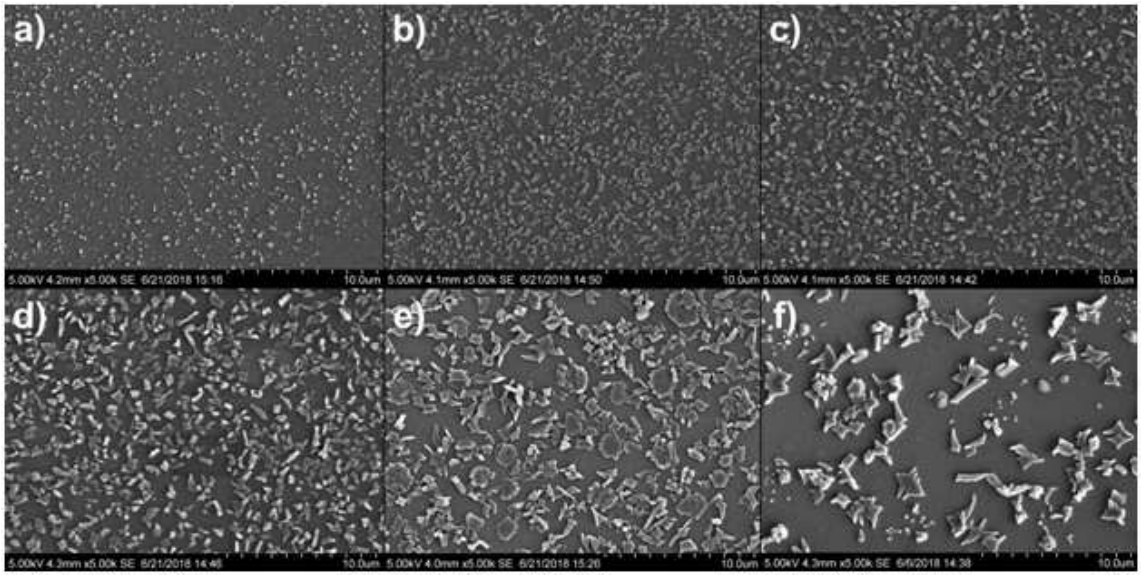

Figure 3.20: MEB-images d'échantillons avec différentes concentrations de produits dans les solvants: a) 1%, b) 3%, c) 5%, D) 8%, e) 10% et f) 15%.

tion de la taille des cristaux de DAST.

Le second matériau est utile pour la fabrication de structures périodiques par transfert photoinduit de cristaux lors de la polymérisation de monomères. Il est préparé à partir d'une solution de DAST liquide (méthanol comme solvant) et de deux monomères: IDA (Isodecyl acrylate) et TMP (trimethylolpropane ethoxylate (1 EO/OH) methyl ether diacrylate). L'analyse a montré que la taille moyenne des cristaux synthétisés est de 1 μm. La meilleure ration entre les monomères IDA et TMP était de 1:1. La température de recuit ne doit pas dépasser 120°.

Les publications concernant ces travaux:

- Pogosian T., Mai T.N., Denisyuk I., Lai N.D. // Synthesis and nonlinear optics characterization of DAST submicron crystals in

polymerized thin films // Proceedings of SPIE - 2018, Vol. 10681, pp. 106811A.

- Pogosian T.N., Denisyuk I.Y., Lai N. // The influence of dimensional parameters of DAST nanocrystals on their linear and nonlinear optical parameters // Optics and spectroscopy, Vol. 126, No. 3, pp. 262-264 (2019)

C – Développement de méthodes de fabrication : Cette partie est axée sur la démonstration des méthodes de fabrication, qui permettent de créer des structures QPM 2D et 3D sur la base de matériaux synthétisés.

La première méthode est l'écriture holographique sur les nanocomposites. Le processus de polymérisation périodique a été réalisé par une configuration holographique simple avec deux faisceaux laser cohérents. La polymérisation des monomères induit un transfert des cristaux de DAST dans les zones sombres. La période de grille était de 5,5 μm. Le temps d'exposition était de 10 min. Après exposition, la diffraction du réseau 1D a été observée à l'œil et au microscope (Figure 3).

La deuxième méthode consiste à écrire directement au laser sur le matériau nanocomposite à base de PMMA. Un laser de 532 nm a été utilisé pour l'ecriture directe par laser parce que cette longueur d'onde appartient au pic d'absorption de DAST. Une grille de 5x5 lignes a été écrit avec une période de 15 μm. Les meilleurs résultats ont été obtenus à une vitesse d'écriture de 10 μm / s et une puissance laser de 35 mW.

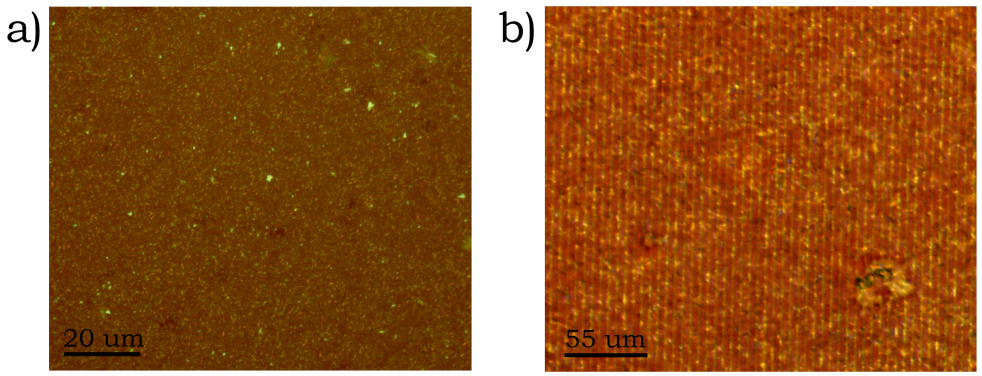

Figure 3.21: Images optiques de: a) échantillon, polymérisé en faisceau laser collimaté uniforme; b) une structure périodique 1D avec une période 5,5 μm.

La taille du spot enregistré est de 1 μm. La Figure 4 présente une correspondance des couleurs du signal de fluorescence après différentes combinaisons de paramètres d'écriture. La différence de signal est due au fait que le rendement quantique de luminescence du dast amorphe est égal à 0,2%, tandis que le rendement quantique de luminescence du cristal est égal à 14-20%.

La troisième méthode est consacrée à la synthèse des cristaux de DAST dans les vides du template SU-8. L'épaisseur d'un échantillon SU-8 était de 2 μm. En utilisant la technique d'interférence, une structure 2D périodique a été fabriquée avec une période de 3 μm. Les vides du template SU-8 ont été remplis avec du matériel de nanocomposition PMMA/DAST. La structure périodique non linéaire a été balayée par un laser de 532 nm pour générer le signal de luminescence, et par un laser de 1064 nm pour générer le signal SH. La Figure 5 montre une structure périodique bien visible formée par le signal SH.

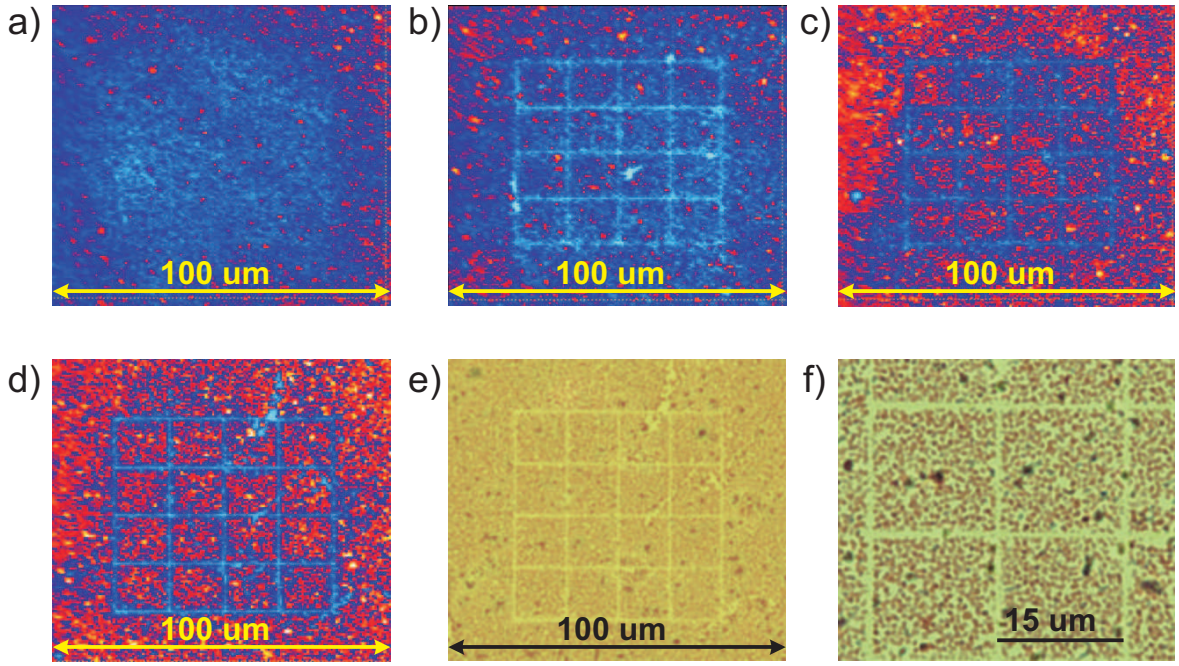

Figure 3.22: Images de fluorescence d'échantillons de DAST après photoblanchiment avec différentes combinaisons de paramètres d'écriture, qui peuvent être présentés comme un couple "puissance-vitesse": a) 1 mW-5 μm / s b) 5 mW-5 μm / s c) 5 mW-10 μm / s d) 10 mW-35 μm / s. e) - f) Image optiques de l'échantillon enregistrées avec une puissance de 10 mW et une vitesse de 35 μm / s et prises par un microscope optique.

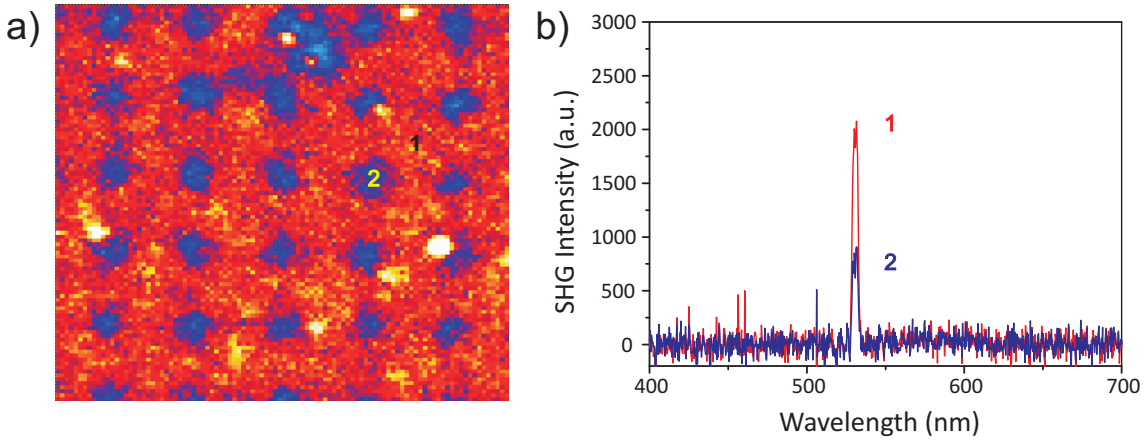

Figure 3.23: a) Image de SH par balayage des plans XY à des positions z fixes et b) spectres SH de deux points de l'échantillon, où la ligne 1 correspond à la zone remplie de DAST et la ligne 2 correspond à la zone SU-8.

Les publications concernant ces travaux:

- Pogosian T.N., Denisyuk I.Y., Lai N. // Controllable synthesis of DAST submicron crystals and their microstructuration by direct laser writing // FIR-LAB 2019 Workshop & RJUSE Symposium proceedings, (2019), pp. 38-39

- Denisyuk I.Y., Ozheredov I., Sinko A., Fokina M., Pogosian T., Ignateva I., Diep Lai N., Ledoux-Rak I. // Optical properties of photobleached DAST molecular crystals in terahertz domain // Journal of Infrared, Millimeter, and Terahertz Waves (2019), accepté pour publication.

Suite à ces travaux, plusieurs perspectives sont proposées:

- Augmentation de l'épaisseur des films PMMA/DAST et construction d'une configuration pour DLW par absorption à deux photons pour fabriquer des structures QPM 3D.

- Fabrication de template 3D SU-8 et examen des limites de la période des structures liées à la possibilité de combler les vides par XX composite.

- Fabrication de structures non linéaires périodiques 2D et 3D par technique d'interférence ou par masque lithographique dans un matériau à base de nanocoposite polymérisable avec des monomères et des cristaux DAST.

université PARIS-SACLAY

ÉCOLE DOCTORALE
Physique et ingénierie : électrons, photons, sciences du vivant (EOBE)

Titre : Structures quasi-accord de phase 3D: étude théorique, élaboration de matériaux non-linéaires, et réalisation des structures en matériau polymère

Mots clés : Quasi-accord de phase, polymère, interférence, génération de seconde harmonique, DAST nanocristal

Résumé : Dans ce travail, nous explorons théoriquement et expérimentalement des structures non-linéaires en trois dimensions (3D). Tout d'abord, nous avons étudié la théorie de quasi-accord de phase (QPM) des structures 3D pour une génération efficace de seconde-harmonique. L'efficacité de la conversion de fréquence est analysée en fonction de plusieurs paramètres, tels que le type de structures, le facteur de remplissage, le motif de maille, etc. Une structure QPM 3D optimale et très proche de la structure expérimentale a été démontrée. Ensuite, nous avons étudié plusieurs méthodes pour synthétiser des matériaux non-linéaires à base de cristaux de DAST. En particulier, la taille de ces cristaux a été optimisée en dessous de micromètre afin de les incorporer facilement dans des structures de polymère. Finalement, nous avons développé plusieurs méthodes pour créer des structures QPM 2D et 3D du type +/0 à la demande. La première méthode est basée sur la technique d'interférence de deux faisceaux laser, qui permet de pousser les cristaux DAST non-linéaires dans les zones sombres de la figure d'interférence. Cette technique rapide mais le contraste de la propriété non-linéaire est faible. La deuxième méthode consiste à utiliser la technique dite écriture directe par laser. Cette méthode permet de blanchir la propriété des cristaux de DAST par l'effet photothermique local. En déplaçant le spot de focalisation du faisceau laser, n'importe quelle structure QPM 2D peut-être réalisée. Finalement, nous avons démontré une méthode rapide permettant d'obtenir des structures QPM 2D et 3D de grande contraste, en remplissant les trous de structures de SU-8, fabriquées initialement par la méthode d'interférence, par les cristaux DAST.

Title : 3D nonlinear quasi-phase matching structures: theoretical analysis, material synthesis and study of polymer-based fabrication technique

Keywords : Quasi-phase matching, polymer, interference, second-harmonic generation, DAST nanocrystals

Abstract : In this study, we investigate theoretically and experimentally 3D quasi-phase matching (QPM) structures. The work focuses on i) mathematical analysis of second-harmonic generation efficiency in 3D QPM lattices, ii) synthesis and analysis of polymers materials with embedded nonlinear submicron particles for fabrication of nonlinear lattices, iii) development of methods for creation of nonlinear 2D and 3D QPM lattices. The purpose of the theoretical part is to define the influence of different parameters of 3D QPM structures on the efficiency of the frequency conversion. In order to conduct our experimental research, we then synthesis two composite materials which consist of polymer matrices with embedded nonlinear submicron DAST crystals. Using these materials, we are capable of creating novel methods of fabrication of 2D and 3D QPM structures. The first method consists of holographically writing a photopolymerizable composite, during which the nonlinear DAST crystals are transferred into the dark zones of the interference pattern. The second method employs the direct laser writing technique to patterning the submicron DAST crystals embedded in polymer matrices, by the photothermal destruction effect. Finally, the third method allows creation of 2D nonlinear lattices by filling voids of SU-8 template with submicrometer DAST crystals.

Université Paris-Saclay
Espace Technologique / Immeuble Discovery
Route de l'Orme aux Merisiers RD 128 / 91190 Saint-Aubin, France